Arab American University

Faculty of Graduate Studies

Methods of formation of Niobium Tin Oxide compound and some related applications

By

Bayan Hosni Naser Kmail

Supervisor

Prof. Dr. Atef Fayez Qasrawi

This Thesis was submitted in partial fulfillment of the requirements for

the Master's degree in Physics

July/2021

Methods of formation of Niobium Tin Oxide compound and some related applications

By

Bayan Hosni Naser Kmail

This thesis was defended successfully on 13th July 2021 and approved by:

Committee members	Signature
1. Supervisor: Prof. Dr. Atef Fayez Qasrawi	.....
2. External examiner: Assoc. prof. Dr. Iyad Saadeddin	.....
3. Internal examiner: Assoc. Prof. Dr. Ahmad Omer	.....

Declaration

The work in this thesis, unless otherwise referenced, is the researcher's own work and has not been submitted elsewhere for any other degree or qualification.

Student's Name: Bayan Hosni Naser Kmail

Signature: Bayan

Date: 30/11/2021

Acknowledgment

Praise to God, who gave me the strength, patience and determination to embark on the journey towards obtaining a master's degree. I am deeply thankful to my supervisor, the honorable Professor. Dr. Atef Qasrawi for his support and encouragement, who gave me much of his time and effort in reading, checking and gave me advice and guidance to do my best. Special thanks to the external examiner, the virtuous Dr. Eyad Saadeddin, and the internal examiner, the virtuous Dr .Ahmad Omar. Thanks a bunch for all the members of physics department in my prestigious university - Arab American University - and to the Ministry of Higher Education- the institution of my work. Words cannot express how much I'm grateful to my parents and my wonderful brothers and sisters for being the first supporters. I will never forget the support offered by the kind assistant Rana Daragmeh and to all lab friends Lara, Walaa, Mayamen and Haneen. As we worked as a family and their presence relieved a lot of pressure. Finally, I am eternally grateful to my colleagues, my friends, to everyone who gave me any kind of help and wished me success in my way.

Abstract

Methods of formation of Niobium Tin Oxide compound and some related applications

In this thesis, we have prepared $SnNb_2O_6$ compounds by three methods. Namely, by the laser welding (LW) technique under N_2 atmosphere, by solid state reaction (SSR) technique and by thermal evaporation (TE) technique. The produced samples are studied by means of X-ray diffraction, impedance spectroscopy and optical spectrophotometry techniques. The preparation method by SSR technique included sintering process at various temperatures in the range of 1000-1300°C for sintering times in the ranges of 2- 6 hrs. The XRD analysis for the samples has shown that; samples prepared by LW and SSR techniques are of polycrystalline nature. On the other hand, deposited Glass/Nb_2O_5/SnO_2 thin films displayed amorphous structure. In general, $SnNb_2O_6$ samples display multiphase structure. The dominant structural phase depends on the preparation technique and/or sintering temperature. It is also observed that, the structural parameters including the crystallite sizes, the microstains, the stacking faults and defect densities are highly influenced by the preparation method. Samples of the largest crystallite size, least strain and least defect density are obtained by the SSR technique at sintering temperature 1300°C for 3 hrs. Single phase of the orthorhombic $SnNb_2O_6$ is achieved by the same method at 1300°C being sintered for 3 hrs. On the other hand, the impedance spectroscopy measurements have shown that samples prepared by LW technique display the highest impedance in the frequency domain of 10-1800 MHz. Negative conductivity is observed for samples prepared by the SSR and LW techniques near 1500 MHz. While the capacitance spectrum of the sample prepared by laser welding technique show resonance – antiresonance phenomena in the microwave frequency

domain. These prepared by SSR and TE techniques showed the same phenomena in the radiowave range of frequency. Modeling of the capacitance and conductivity spectra indicated the domination of quantum mechanical tunneling and correlated barrier hopping conduction in the samples. The optical measurements which were possible for samples prepared by TE technique indicated the existence of two energy band gaps being dominant above and below 3.0 eV, respectively. In addition, the Drude – Lorentz modeling of the conductivity spectra of the samples prepared by TE technique have shown that the drift mobility of thin film samples increased upon stacking of Glass/Nb_2O_5 with SnO_2. The stacked layers of the films display plasmon frequency values that suits for microwave resonators.

List of contents

List of tables

List of Figures

List of symbols

Symbol	Symbol Meaning
Nb_2O_5	Niobium oxide
SnO_2	Tin oxide
$SnNb_2O_6$	Niobium Tin oxide
SSR	Solid state reaction technique
LW	laser welding
TE	thermal evaporation technique
ITO	Indium Tin Oxide
TCO	transparent conducting oxides
NDC	negative differential conductance
XRD	X-Ray diffraction
m*	effective Mass
θ	Bragg angle
D	Crystallite Size
β	The peak broadening at full width half maximum peak in radians
δ	Dislocation density
ε	Strain
α	Absorption Coefficient
ε_r	The real part of the dielectric constant
ε_{im}	The imaginary part of the dielectric constant
ω_{pe}	Electron-plasmon frequency
ε_{eff}	effective dielectric constant
ε_s	The permittivity of semiconductor
T%	Transmitance
R%	Reflectance
ω	Angular frequency
CBH	Correlated Barrier Hopping
QMT	Quantum Mechanical Tunneling

Chapter One

Introduction

Ceramic technology is nowadays attracting a lot of attention due to the growth in the demand for light weight and multifunctional electronic devices. Bismuth-zinc niobium oxide (BZN) pyrochlore ceramics are the most famous and important compound form in the BZN system. As an example, $Bi_{1.5}\ Zn_{0.92}\ Nb_{1.5-6x/5}O_{6.92}$ pyrochlore ceramics doped with tungsten (W-BZN) which was prepared by the solid state reaction technique designated as radiowave / microwave band pass / reject filters , is also recommended for use as noise reducers and microwave signal receivers [1]. In addition, the low dielectric loss of the dielectric constant , the stability of the dielectric constant and the low sintering temperature of $Bi_{1.5}\ Zn_{0.92}\ Nb_{1.5-x}\ Sn_xO_{6.92-x/2}$, for Sn contents in the range of $0.00 < x < 0.60$ make the ceramic compound suitable for wireless technology [2]. Another group of ceramics are Perovskite ceramics. Example of the pervoskite ceramics is $Ba(Zn_{1/3}Nb_{2/3})O_3$ (BZN) ceramics, which are gaining the focus of research due to their multiple functions. $(Ba_{0.3}Sr_{0.7})(Zn_{1/3}Nb_{2/3})O_3$ ceramic in the form of thin films prepared by sol–gel technique play an important role in the fields of radars, satellite and mobile communication systems [3]. Moreover, the doping $Ba(Zn_{1/3}Nb_{2/3})O_3$ Perovskite ceramic with antimony (Sb) prepared by solid state reaction, causes a decreases in the dielectric constant value and exhibits a high dielectric quality factor which make it suitable for radiowave resonators [4].

On the other hand, transparent conducting oxide (TCO) have attracted huge attention due to the expanding demand for transparent flexible electrodes in optoelectronic devices such as solar cells, batteries, light emitting diodes (LEDs) and window coating [5,6,7]. TCO are materials which show both high conductivity and transparency (largely transparent to

visible light). Indium oxide (In_2O_3), zinc oxide (ZnO) and Titanium Oxide (TiO_2) are identified as a metallic oxide system and are attractive TCO materials used in optoelectronic devices [8]. In addition, tin (IVA) oxide (SnO_2) is a famous member of the TCO. SnO_2 thin films have semiconductor and rutile structure with a wide band gap [9]. Moreover, widespread availability, low cost, chemical, mechanical stability of doped SnO_2 [10]. SnO_2 has many unique features such as the optical transmittance in the visible range, low electrical resistance [11, 12], resistance to corrosion [13], chemical inertness and mechanical hardness [14]. These characteristic allowed it to be used in solar cells, gas sensor, alternatives to carbon blacks at a Proton-Exchange Membrane Fuel Cell (PEMFC) cathode and display devices, respectively. Niobium (VB) pentoxide Nb_2O_5 is another important metal oxide component which is used in many technological applications such as optical smart windows, display devices, gas sensing, electrochromic applications and photocatalytic. The usability of the compound in these applications is due to its many unique physical and chemical characteristics, such as high refractive index, wide energy gap and thermal and chemical stability [15, 16].

An improvement in the electrical and optical properties of semiconductors can be obtained through a variety of strategies such as the dopant concentration, preparation parameters such as annealing temperature and deposition and preparation techniques. All of them have an effect on the properties of the resulting compound. For example, there are many experimental techniques for thin-film deposition such as DC magnetron sputtering technique, pulsed laser deposition technique, sol – gel , rf sputtering technique [15,16] and thermal evaporation technique [17]. On the other hand, ceramics can be prepared by flux technique [18], hydrothermal synthesis technique [19], solvothermal synthesis technique

[20], precipitation technique [21] and solid state reaction technique [4]. Binary targets of SnO_2 and Nb_2O_5 are employed to fabricate $SnNb_2O_6$ thin films on indium tin oxide (ITO) substrates by pulsed-laser deposition (PLD) method. The resultant polycrystalline $SnNb_2O_6$ have proven the efficiency for use as a photoanode in the photoelectrochemical cell [22]. Furthermore, a heterojunction is formed between Nb_2O_5 and SnO_2 in the Pt-Nb_2O_5-SnO_2 ternary composite ceramics. The composite ceramic is prepared by pressing and sintering process of mixture of SnO_2 nanoparticles, Nb_2O_5 and Pt particles after dispersing in deionized water, whereas Nb_2O_5 proved to have good effects on the hydrogen sensing characteristics of the Pt-SnO_2 system [23]. The versatile Nb_2O_5/SnO_2 heterostructure was synthesized by the hydrothermal method. The heterostructure can be used as different forms of environmental treatment such as water treatment [24].

The Increase in the use of display devices and demand for renewable energy resources, Lithium batteries, microwave cavities, wireless communications and other optoelectronic and microelectronic applications motivated us to use two of these Oxide semiconductors SnO_2 and Nb_2O_5 as raw materials to produce a new class of TCO. Namely, Nb_2O_5/SnO_2 stacked layer thin films are prepared by thermal evaporation technique under inert gas, high vacuum pressure, and oxygen medium, and to produce polycrystalline $SnNb_2O_6$ powder compounds by solid state reaction technique. As a new method for preparing this compound, laser welding technique will also be employed. The effect of the preparation technique on the structural properties of the niobium tin oxide will be investigated by the X-ray diffraction technique. Particularly, the effect of the preparation technique on the crystal structure, lattice parameters, crystallite size, defect density, microstrain and stacking faults will be studied. Moreover, the alternating current conduction mechanism in the

samples will be investigated by the impedance spectroscopy technique. This technique will provide information about capacitance, conductance and impedance spectral response to identify possible electronic applications of the produced compound. Furthermore, the effect of the preparation technique on the electrical conductivity at room temperature will be studied. Finally, the optical properties of the stacked layers prepared by thermal evaporation technique will be studied to determine the possible optoelectronic applications of the thin film.

Five chapters will be included in the thesis. First, introduction about our work. The theoretical background of the basic mathematics used to analyze the results will be discussed in the second chapter. Details and procedures for the experiments will be discussed in chapter Three. The fourth chapter will include the results of XRD diffraction, impedance, electrical and optical measurements of samples prepared using the three different techniques. Finally, Chapter Five will contain concluding remarks on our work.

Chapter Two

Theoretical Background

2.1: X-ray diffraction

X-ray diffraction is a powerful technique used to discover the nature of materials whether they are crystalline or amorphous. Provides information on crystal structures, phases and preferred crystal orientations. When an X-ray beam is scattered at specific angle from a set of lattice planes in a sample and a constructive interference occurs, an XRD peak is produced. The pattern of the XRD peaks is a fingerprint of the periodic arrangements of atoms of a given material [25]. XRD allow determining the interplaner spacing between atomic planes through Bragg reflection condition [26].

2.1.1: Crystal structures

Crystal structure is a description of the way atoms, ions, or molecules are arranged in a crystalline substance. The smallest group of particles that make up an ordered pattern with full symmetry is known as a unit cell. The unit cell is defined by three lattice constants (a, b, c) and three angles (α, β, γ). Fourteen three-dimensional configurations of Bravais lattices distributed over seven different types of crystal systems are presented in Table 2.1 with their conditions [27].

The orientation of the crystalline planes represented by (Miller indices (hkl)) is determined by how the plane intersects the main crystalline axes of the solid.

Table 2.1: 3-D crystal structures for solid state materials and their conditions.

Crystal structure	Lattice constant	Angle	# of Braves lattice
Triclinic	$a_1 \neq a_2 \neq a_3$,	$\alpha \neq \beta \neq \gamma \neq 90^o$	1
Monoclinic	$a_1 \neq a_2 \neq a_3$,	$\alpha = \beta = 90^o \neq \gamma$	2
Orthorhombic	$a_1 \neq a_2 \neq a_3$,	$\alpha = \beta = \gamma = 90^o$	4
Tetragonal	$a_1 = a_2 \neq a_3$,	$\alpha = \beta = \gamma = 90^o$	2
Cubic	$a_1 = a_2 = a_3$,	$\alpha = \beta = \gamma = 90^o$	3
Trigonal	$a_1 = a_2 = a_3$,	$\alpha = \beta = \gamma < 120^o \neq 90^o$	1
Hexagonal	$a_1 = a_2 \neq a_3$,	$\alpha = \beta = 90^o$, $\gamma = 120^o$	1

2.1.2: Structural parameters

The Structural parameters, crystallite size (D), microstrain (ε), dislocation density (δ) and stacking faults (SF %) are determined with the help of maximum peak broadening width (β) of the most intensive peak.

Crystallite size and Scherrer's formula

X-ray diffraction is a conventional method for determining the mean size of crystallites in polycrystalline materials. Crystallite size is calculated according to the Scherrer's formula [28, 29, 30].

$$D = \frac{0.94\,\lambda}{\beta \cos(\theta)} \tag{2.1}$$

with λ being the XRD wavelength, β is the broadening width of the maximum peak or the full width at half maximum of the diffraction peak (FWHM) and θ is the Bragg's angle.

Microstrain

Strain is the deformation caused by the relative displacements of atoms that affects the lattice constant [31]. It is defined by the relation:

$$\varepsilon = \frac{\beta}{4\tan(\theta)} \tag{2.2}$$

Two types of strain can be found in the crystal; uniform strain (elastic deformation) and non-uniform strain (plastic deformation) as shown in Fig 2.1

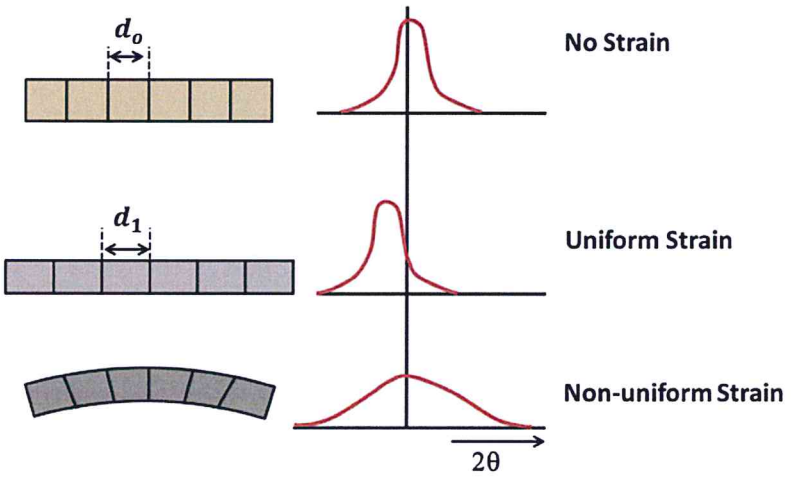

Fig 2.1. Effect of lattice strain on diffraction peak position and width.

Dislocation density

The Dislocation density is the total length of dislocation line per unit area of the crystal (lines/cm^2) [32]. It can be calculated from the following equation [30]:

$$\delta = \frac{15\,\varepsilon}{aD} \tag{2.3}$$

Where a is the lattice constant along the a – axis.

Stacking faults

Stacking faults is defined as a break in the normal sequence of stacking in the crystal [33] or defined as a type of planar defect in a crystal structure. It is determined by the relation [30]:

$$SF = \frac{2\pi^2\beta}{45\sqrt{3\tan(\theta)}} \tag{2.4}$$

2.2: AC capacitance

To explain the discontinuity in the value of the alternating current capacitance (resonance and anti-resonance phenomena) determined using the impedance spectroscopy measurement, Ershov et al model [34] and the modified Ershov model (Ershov- Qasrawi model) were used [35,36]. The Capacitance is defined as:

$$C(\omega) = C_o + \frac{a_1\tau_1}{1+(\omega-\omega_1)^2{\tau_1}^2} - \frac{a_2\tau_2}{1+(\omega-\omega_2)^2{\tau_2}^2} \tag{2.5}$$

In another form:

$$C(\omega) = C_o + C_1 \tag{2.6}$$

Where C_o is the geometrical capacitance and C_1 is the relaxation part of capacitance.

ω is the angular frequency.

τ_1 and τ_2 are the relaxation time of electrons and holes, respectively. a_1 and a_2 are the fitting parameters (pre-exponential values) in F/s, which is defined as the rate of change of dynamic capacitance with time.

ω_1 and ω_2 are the plasmon frequencies for n-type and p-type material, respectively.

Equation (2.5) shows that the capacitance gives negative and positive values in cases where holes or electrons dominate, respectively.

2.3: Alternating current conduction mechanisms

Conductivity can be obtained from the conductance (G) according to the relation [37]:

$$\sigma = \frac{L\,G}{A} \tag{2.7}$$

Where σ is the conductivity, G is the measured conductance, A is the cross sectional area of the sample and l is the length of the conductor.

Frequency-dependent (AC) conductivity arises when a semiconductor or insulator is imposed to an AC signal. The behavior of frequency-dependent conductivity can be attributed to two distinct processes of alternating current mechanisms, namely, quantum mechanical tunneling and correlated barrier hopping, or a combination of the two mechanisms.

2.3.1: Quantum mechanical tunneling (QMT) conduction mechanism

The AC conductivity can be written in the following form according to published theories [35,38]

$$\sigma(\omega) = A\,\omega^{s} \tag{2.8}$$

Where A is a temperature dependent constant, ω is the frequency of the AC signal, $s \leq 1$ is the exponent constant defined by,

$$s = \frac{d\,ln\sigma(\omega)}{d\,ln\omega} \tag{2.9}$$

If the value of the exponent is nearly equal unity, then the AC conductivity is linearly dependent on the frequency.

After some derivations, the relaxation time (τ) is given by the relation

$$\tau = \tau_o e^{\xi} \tag{2.10}$$

Where the relaxation time is the time required for the system to go back to its equilibrium after perturbation, τ_o is a characteristic relaxation time. $\tau_o = \frac{1}{\upsilon_{ph}}$, υ_{ph} is the phonon frequency. ξ is a random variable whose value determines the type of AC conduction mechanisms. For quantum mechanical tunneling (QMT), ξ is given by $\xi = 2\alpha R$, where R is the intersite separation and α is a constant used to describe the localized state at each site. The AC conductivity according to the (QMT) model is determined by

$$\sigma(\omega) = \frac{\pi^4}{24} e^2 \, k_B T \alpha^{-1} [N(E_F)]^2 \, \omega \, {R_\omega}^4 \qquad (2.11)$$

Where $N(E_F)$ is the density of states at the fermi level.

α^{-1} is the spatial decay parameter that is nearly constant for all sites and it is equal to 0.1Å , k_B is Boltzmann constant, e is the charge of electron, T is the temperature in kelvin. R_ω is the hopping distance at a given frequency ω, which is equal to:

$$R_\omega = \frac{1}{2\alpha} \ln\left(\frac{1}{\omega\tau_0}\right)$$

Taking the logarithm and then executing the derivative for both sides of equation 2.11, the value of the exponent constant according to the quantum mechanical tunneling model is given by following equation:

$$s = 1 - \frac{4}{\ln\left(\frac{1}{\omega\tau_0}\right)} \qquad (2.12)$$

from equation (2.12) $\frac{4}{1-s} = \ln\left(\frac{1}{\omega\tau_0}\right)$, $\frac{4}{1-s} = -\ln(\omega\tau_0)$ then $\omega\tau_0 = e^{\frac{4}{s-1}}$

2.3.2: Correlated barriers hoping (CBH) conduction mechanism

For the Correlated barriers hoping (CBH) model [35,39], the random variable ξ from equation (2.10) is given by $\xi = W_h/k_B T$, where W_h is the hopping barrier height.

The AC conductivity in the case of CBH mechanism is given by the relation:

$$\sigma_{QBH}(\omega) = \sigma_H(\omega) + \frac{\sigma_L(\omega) - \sigma_H(\omega)}{1+\omega^2\tau^2} \quad (2.13)$$

Where the subscript symbols H means conductivity at high frequency and L means conductivity at low frequency.

In the case where two AC conduction mechanisms QMT and CBH are dominants, the total AC conductivity is calculated according to the relation:

$$\frac{1}{\sigma_{tot}} = \frac{1}{\sigma_{QMT}} + \frac{1}{\sigma_{CBH}} \quad (2.14)$$

Where σ_{tot} is the total conductivity.

2.4: Impedance measurement (RLC circuit)

An RLC circuit is an electrical circuit consisting of a resistor (R), an inductor (L), and a capacitor (C) connected in series or in parallel. A series RLC circuit has a single loop with the same value of current flowing through the circuit components R, L and C. The source voltage V_s drops across each circuit components by the values V_R, V_L and V_C values for R, L and C, respectively.V_R is in-phase with current, while V_L and V_C are out of phase and in opposite direction to each other as shown in Fig 2.2(a). Where V_L leads current by 90° and V_C lags current by 90° [40]. The magnitude of source voltage V_s can be calculated by applying Kirchhoff's voltage law which gives:

$$\mathbf{V_S - V_R - V_L - V_C = 0} \quad (2.15)$$

$$V_S - IR - L\frac{dI}{dt} - \frac{Q}{C} = 0 \quad (2.16)$$

$$V_S = IR + L\frac{dI}{dt} + \frac{Q}{C} \quad (2.17)$$

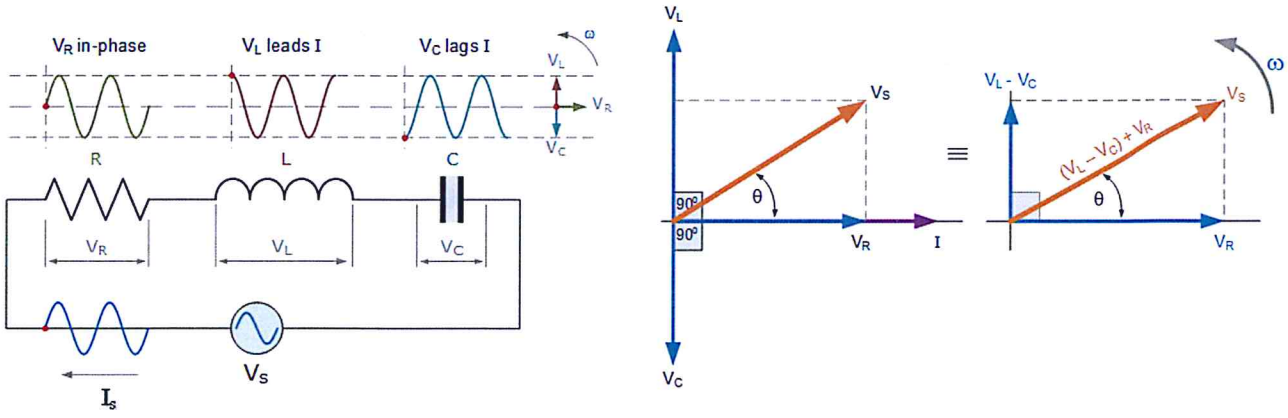

Fig 2.2. (a) The series RLC circuit (b) phasor diagram for a series RLC circuit.

Depending on the voltage triangle of the series RLC circuit as shown in Fig 2.2(b) V_S is equal to.

$$V_S = \sqrt{V_R^2 + (V_L - V_C)^2} = I.\sqrt{R^2 + (X_L - X_C)^2} = IZ \quad (2.18)$$

As a final result:

$$Z = \sqrt{R^2 + (X_L - X_C)^2} \quad (2.19)$$

Where I is the current, X_L inductive reactance, X_C capacitive reactance and Z is the impedance.

2.5: Optical properties of semiconductors

From the optical transmittance (T) and optical reflectance (R) measurement, the absorption coefficient spectra (α) is calculated and analyzed to understand the band structure and energy band gap. The dielectric constant (ε) is evaluated to determine the optical conductivity and critical energies of resonance. When the light is incident on optical medium, some of the light is reflected, transmitted and /or the remaining part is absorbed by the material atoms.

2.5.1: Absorption coefficient (α)

Absorption coefficient is the amount of light that is absorbed in the optical medium within a certain thickness; the absorption process occurs when the electrons of an atom make a transition from occupied lower state to the empty upper state.

Based on Beer's law the absorption coefficient can be determined [41]:

$$I(z) = I_o e^{-\alpha z} \tag{2.20}$$

Where z is the material thickness, I_o is the intensity of light at z = 0 and α is the frequency dependent absorption coefficient. ($e^{-\alpha z}$) is the exponential appears due to the decreased in light intensity during the absorption process .The transmissivity of light in the optical medium can be calculated according to the relation [41]:

$$T = (1 - R_1)(1 - R_2)e^{-\alpha z} \tag{2.21}$$

Where R_1 and R_2 are the reflections of the first and second layers, and the term ($e^{-\alpha z}$) results from the absorption process according to Beer's law. The terms $(1 - R_1)$ and $(1 - R_2)$ represent the transmission of the first and second layers of the optical medium, respectively.

If z = d, where d being the film thickness, then α becomes,

$$\alpha = -\frac{1}{d} \ln\left(\frac{T}{(1-R_1)(1-R_2)}\right) \tag{2.22}$$

Electronic band structure

According to tight binding models, when a large number N of identical atoms come close to each other to form a solid, the coulomb interaction between the atom cores and the electron splits the energy levels, spreading them into bands. Each state of given quantum number of the free atom is spread in the crystal into a band of energies. These bands are valence band,

conduction band separated by an energy gap as shown in Fig 2.3. The width of the band is proportional to the strength of the overlap interaction between neighboring atoms [42, 43].

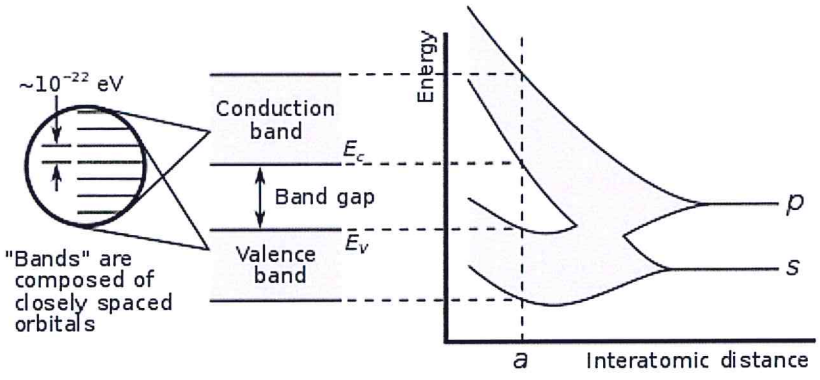

Fig 2.3. Forming the electronic band structure of solids.

2.5.2: Energy band gap

The energy band gap or "forbidden region" represents the minimum energy required to excite an electron from a state in the valance band to a state in the conduction band where it can participate in conduction. There are two basic types of band gap which are "direct band gap "and "indirect band gap"[44].

The maximum energy state in the valence band and the minimum energy state in the conduction band are characterized by (k-vector) which indicates a particular crystal momentum. If the angular momentum of electrons and holes are the same (k-vectors are the same), then the material has a "direct band gap" and the electron can directly make a transition from conduction band to valence band and emits a photon. An "Indirect band gap" is dominant if k-vectors differ at the maximum valence band and minimum conduction band. In this case, photon cannot be emitted until the electron transfer momentum to the crystal lattice. This process must be mediated by a phonon because photon's momentum is

less than the crystal's momentum. Fig 2.4 represents the direct and indirect energy gap photon emission process.

Direct and indirect transition can be allowed or forbidden transition. Allowed transition occurs if the momentum matrix characterizing the transition is different from zero. This means that enough energy is given to the electron. The forbidden transition occurs if the momentum matrix elements are equal zero.

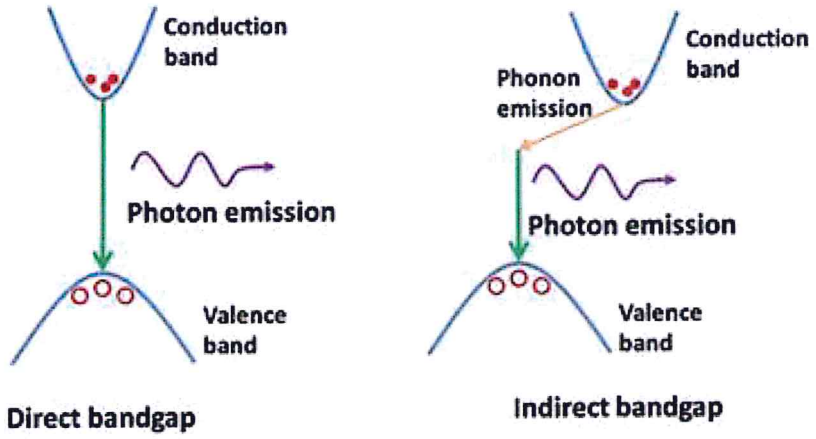

Fig 2.4. Direct and indirect band gap of semiconductors.

2.5.3: Energy gap and Tauc's equation

In order to determine the type of optical transitions, The Tauc's equation which is given by the following relation can be applied [45]

$$(\alpha E)^p = A\left(E - E_g\right) \tag{2.23}$$

Where A is a constant, α is the absorption coefficient, E is the energy of the incident light and E_g is the energy band gap. p is an index characterizing the nature of the transition, which can take the values $2, \frac{2}{3}, \frac{1}{2}, \frac{1}{3}$ related to the direct allowed, direct forbidden, indirect

allowed and indirect forbidden transitions, respectively. The common way to determine the value of the optical energy gap is to plot $(\alpha E)^p$ versus photon energy. The appropriate value of p is used to get best linear fit with the widest range of data, and then the value of energy gap will be determined at the E- axis crossing.

2.5.4: Band tails and Urbach's rule

Band tails are energy levels that extend from the valence band and conduction band into the band gap, meaning that the band tails are formed within the band gap as shown in Fig 2.5. The optical transition occurs between the extended state and the localized state.

In the low absorption region and near the band edge, the probability of band tails is high, and the absorption coefficient can be given by the following relation according to the Urbach's rule [45]:

$$\alpha = \alpha_o e^{(\frac{E}{E_e})} \tag{2.24}$$

α_o is a constant and E_e is the band tail energy. The absorption coefficient is proportional exponentially to the energy of the incident light.

Taking the logarithm of both sides of the equation (2.24), we get

$$\ln \alpha = \ln \alpha_o + \left(\frac{E}{E_e}\right) \tag{2.25}$$

The band tail energy can be determined from the linear slope value of $\ln \alpha$- E variation.

Where $E_e = \frac{1}{Slope}$.

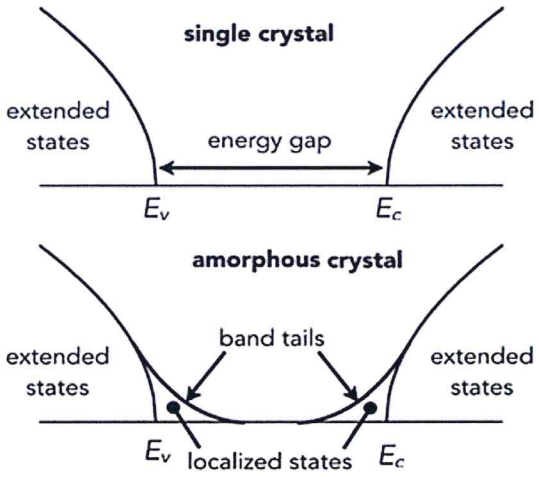

Fig 2.5. Formation of localized states within the energy band gap of the amorphous crystal.

2.6: Dielectric constant

The dielectric constant ε(ω) represents the amount of electrical potential energy stored in a material under the influence of an electric field or light. To arrive at the formula for the dielectric constant, a complex refractive index must be entered, where the refractive index describes the propagation of light in optical materials. The complex refractive index is defined by the relation [46, 47],

$$\tilde{N}_{complex} = n + i\tilde{k} \tag{2.26}$$

Where n is the real part of refractive index, which represent the refraction of light and $\tilde{k}$ is the extinction coefficient which represent the wave's attenuation, so it vanishes for lossless material. The complex refractive index can also be defined as:

$$\tilde{N}_{complex} = \sqrt{\mu\varepsilon_{complex}} \tag{2.27}$$

Where μ is the magnetic permeability and ε is the complex dielectric function. For non- magnetic materials $\mu = 1$. Hence the complex refractive index can also be defined as

$$\tilde{N}_{complex} = \sqrt{\varepsilon_{complex}} \tag{2.28}$$

After squaring both sides of the equation (2.26) and equation (2.28)

$$\left(\tilde{N}_{complex}\right)^2 = \varepsilon_{complex}=(n + i\tilde{k})^2 \tag{2.29}$$

As a result

$$\varepsilon_{complex} = n^2 - \tilde{k}^2 + i2n\tilde{k} \tag{2.30}$$

Alternatively, the dielectric constant formula states that

$$\varepsilon_{complex} = \varepsilon_r + i\varepsilon_{im} \tag{2.31}$$

Where ε_r is the real and ε_{im} is the imaginary part of the dielectric constant.

Comparing equation (2.30) and equation (2.31), ε_r and ε_{im} are given by the following formula:

$$\varepsilon_r = n^2 - \tilde{k}^2 \tag{2.32}$$

$$\varepsilon_{im} = 2n\tilde{k} \tag{2.33}$$

The relation between $\tilde{k}$ and α is given by,

$$\tilde{k} = \frac{\lambda\alpha}{4\pi} \tag{2.34}$$

As a result and after let $\varepsilon_{complex} = \varepsilon_{eff}$ and $n = \sqrt{\varepsilon_{eff}}$, where ε_{eff} is the effective dielectric constant, the real and imaginary parts of the dielectric constant are given by:

$$\varepsilon_r = \varepsilon_{eff} - \left(\frac{\alpha\lambda}{4\pi}\right)^2 \tag{2.35}$$

$$\varepsilon_{im} = 2\sqrt{\varepsilon_{eff}}\ \frac{\alpha\lambda}{4\pi} \tag{2.36}$$

The relation between the normal incident reflectivity and the dielectric constant which is useful in optical calculations,

$$R = \left|\frac{1-\tilde{N}_{complex}}{1+\tilde{N}_{complex}}\right|^2 = \frac{1+n^2-2n+\tilde{k}^2}{1+n^2+2n+\tilde{k}^2} = \frac{(1-n)^2+\tilde{k}^2}{(1+n)^2+\tilde{k}^2} \quad (2.37)$$

In the case of a strongly absorbed medium (large value of absorption coefficient) with a large value of n *and* $\tilde{k}$ ($n = \tilde{k} >> 1$), equation (2.37) becomes

$$R = \frac{n^2-2n+\tilde{k}^2}{n^2+2n+\tilde{k}^2} \quad (2.38)$$

Re-arrange equation (2.38), one can get

$$Rn^2 + 2Rn + R\tilde{k}^2 = n^2 - 2n + \tilde{k}^2 \quad (2.39)$$

$$(R-1)n^2 + 2(R+1)n + (R-1)\tilde{k}^2 = 0 \quad (2.40)$$

$$n^2 + \frac{2(R+1)}{(R-1)}n + \tilde{k}^2 = 0 \quad (2.41)$$

Using the relation $\left(n = \frac{-b\mp\sqrt{b^2-4ac}}{2a}\right)$ to solve a quadratic equation

$$n = -\frac{(R+1)}{(R-1)} \mp \sqrt{\left(\frac{R+1}{R-1}\right)^2 - \tilde{k}^2} \quad (2.42)$$

But let $n = \sqrt{\varepsilon_{eff}}$, so,

$$\sqrt{\varepsilon_{eff}} = -\frac{(R+1)}{(R-1)} + \sqrt{\left(\frac{R+1}{R-1}\right)^2 - \tilde{k}^2} \quad (2.43)$$

$$\sqrt{\varepsilon_{eff}} = -\frac{(R+1)}{(R-1)} - \sqrt{\left(\frac{R+1}{R-1}\right)^2 - \tilde{k}^2} \quad (2.44)$$

Therefore the effective dielectric constant ε_{eff} can be extracted from the reflectance spectrum R and the absorption coefficient α.

Chapter Three

Experimental Details

Niobium (VB) oxide (Nb_2O_5) and Tin (IVA) oxide (SnO_2) powder are used to prepare samples using three different preparation technique namely laser welding technique, solid state reaction technique and thermal evaporation technique.

3.1: Sample preparation by laser welding technique

In the laser welding technique, equal amounts of Tin Oxide (SnO_2) and Niobium Oxide (Nb_2O_5) are used as source material to prepare the $SnNb_2O_6$ sample. The mixture consisting of 0.5 g of high purity Nb_2O_5 powder (99.9985%) and 0.5 g of high purity SnO_2 powder (99.99%) is ground in a mortar for 40 minutes. The iWELD device shown in Fig 3.1(a) is used to produce $SnNb_2O_6$ alloy. The iWELD is described as a hot light power tool with a wavelength of 1064 nm. The maximum output pulse energy is 150 J, the maximum peak power is 10.0 kW with an average power of 60 W, the pulse length range is 0.5-50 ms, the pulse frequency range is 0.5 - 30 Hz, and the beam diameter range is 0.05 - 2.00 mm. During the preparation, the ground mixture is placed in a small container and exposed to a hot laser beam as shown in Fig 3.2(a). The process is completed as shown in Fig 3.1(b) at 211 Volts, pulse width of 2.3 ms, frequency of 5 Hz, which means that every 0.2 seconds the sample is hit by the hot laser beam, beam diameter of 2 mm, and the performance of the pulse is basic. The process was completed in gas medium (N_2) to prevent further oxidation of the sample. Fig 3.2(b) represents the resultant sample while it is still under laser bombardment.

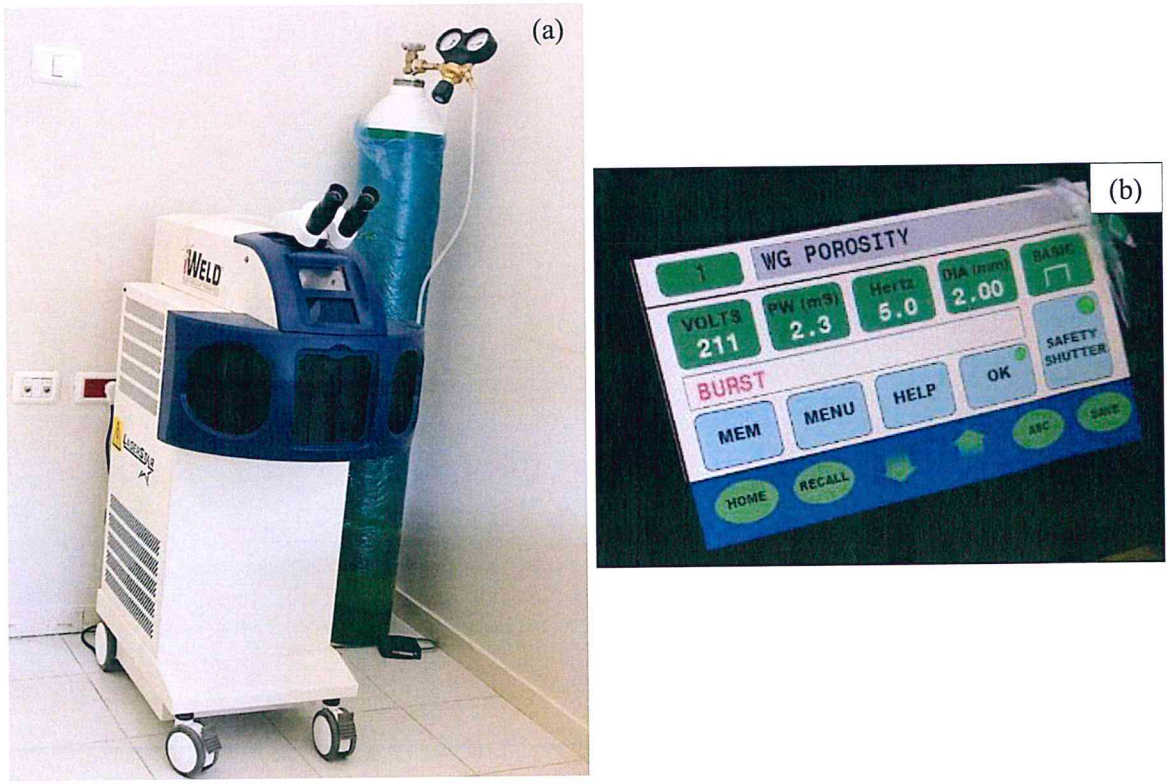

Fig 3.1. (a) The optical image of the I WELD LASER device (b) Laser pulse settings used in the alloying process.

Small solid grey particles and powders of $SnNb_2O_6$ were produced from the process. The bulky sample shown in Fig 3.2(c) was used for all measurements except for the optical measurement. The powder was compressed at 220 bar by the hydraulic press shown in Fig 3.3. The compressed sample shown in Fig 3.2(d) was used for X-ray diffraction measurements. On the other hand, for comparison, the SnO_2 and Nb_2O_5 powders which were not treated were compressed under pressure of 200 bar. The pressed samples shown in Fig 3.4 were used for X-ray diffraction measurements.

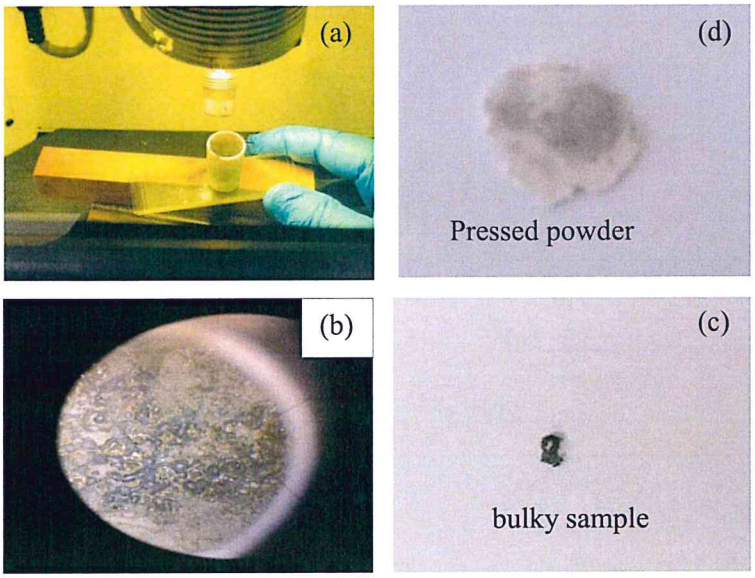

Fig 3.2. (a) Expose of the sample to the pulse laser (b) the resultant sample under laser bombardment before it is separated (c) the solid grey sample and (d) the compacted powder produced by the laser welding technique.

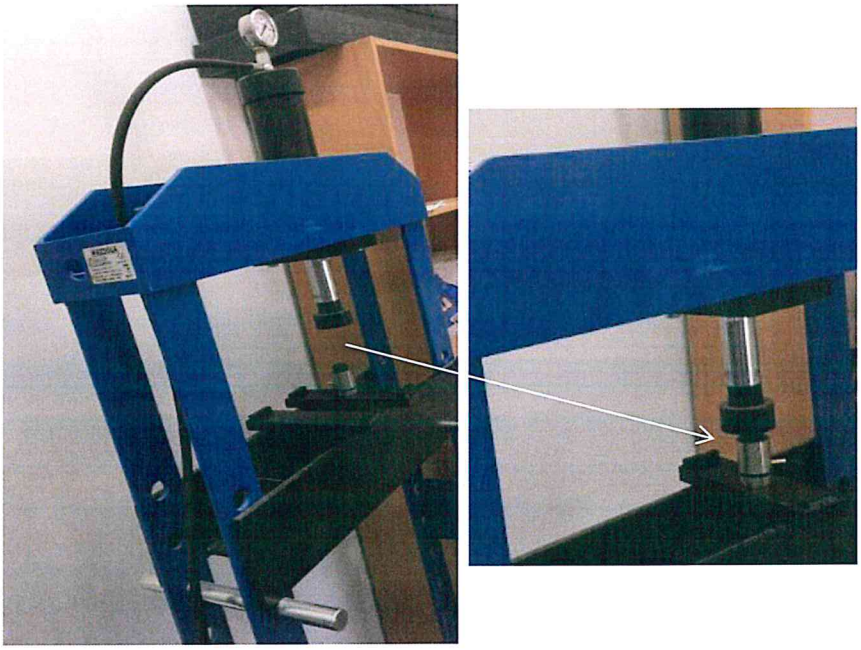

Fig 3.3. The optical image of the hydraulic press used to compress powders.

Fig 3.4. The optical image for Nb_2O_5 and SnO_2 powders after being compressed at 200 bar by a hydraulic press.

3.2: Sample preparation by solid state reaction (SSR) technique

The powder of $SnNb_2O_6$ ceramic was synthesized by solid state reaction technique at high temperatures. The Stoichiometric mixtures of Nb_2O_5 and SnO_2 were ground by a gate mortar for 20 min and then mixed in a ball milling machine containing ethanol (Fig 3.5) for 4 hrs in a medium filled with eight lead balls (1.01 mm diameter). The mixed powder is, then, placed in a small container and then calcined and dried for 4 hrs at 200°C in a HERATHERM Oven which is shown in Fig 3.6 (a). The calcined powder was milled again in mortar and sintered at 1000 °C for 2 hrs in a Nabertherm Furance shown in Fig 3.6(b). The resulting sintered powder is pressed into a disc of 1.45 mm thick and 12.78 mm in diameter at 250 bar by a hydraulic press. The optical image of the sample is shown in Fig 3.7(a). Four steps of the sintering process of pressed ceramic powder are realized. Those are 1100 °C for 3 hrs, 1200 °C for 3 hrs, 1300 °C for 3 hrs and 1300 °C for 6 hrs. After the last step of sintering, the sample took on a gray color as shown in Fig 3.7(b). For each heating cycle, the XRD patterns were recorded.

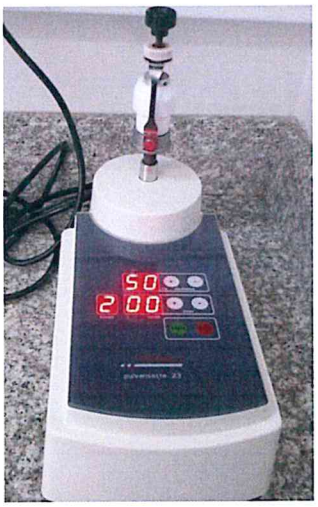

Fig 3.5. Optical image of ball milling machine.

Fig 3.6. (a) Optical image of HERATHERM Oven and (b) Nabertherm Furance.

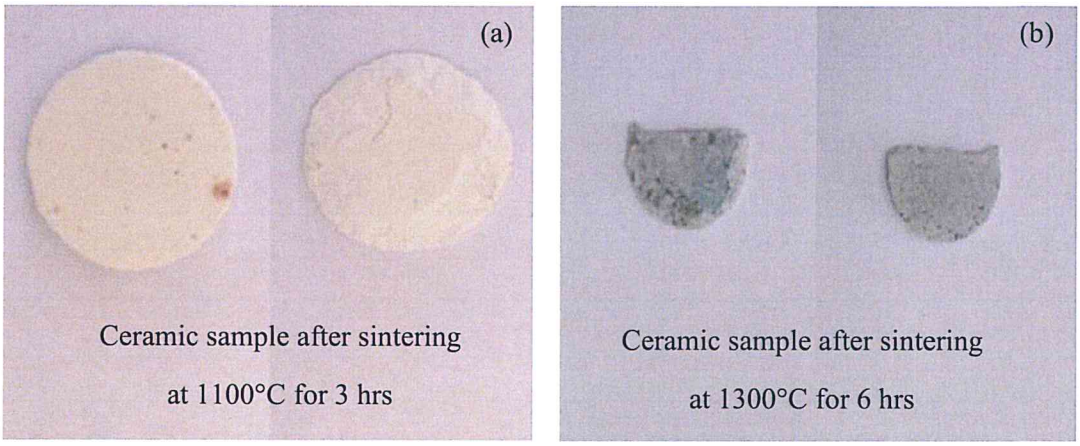

Fig 3.7. (a) The optical image of ceramic sample after sintering at 1100°C for 3 hrs and (b) ceramic sample sintered at 1300°C for 6 hrs.

3.3: Samples preparation by thermal evaporation technique

In this section, we discuss the method of preparing thin films onto glass substrates. The section includes the glass cleaning and thermal evaporation process.

3.3.1: Glass substrate cleaning

Glass slides of dimensions of 7.5× 2.5 cm^2 are used as a thin film substrate. The glass substrate was carefully cleaned to remove dust and contaminants from the substrate surface before use. Firstly, the glass substrates are washed with distilled water and then immersed in 70% Ethyl-alcohol and heated to 70 °C for 20 minutes using an ultrasonic resonator. Secondly, the ultrasonically cleaned glass is again re-washed with alcohol and dried with a glass tissue. Finally, the clean glass is visually inspected to ensure that there are no scratches on its surface and that it is ready to be used as a thin film substrate without rough surfaces.

3.3.2: Evaporating process and thin film preparation

Thermal evaporation (TE) technique was used to prepare thin films of Nb_2O_5, SnO_2 and Nb_2O_5/SnO_2 on glass substrates and Nb_2O_5/SnO_2 on commercial indium tin oxide (ITO) substrates. ITO is a transparent and conductive layer that has a high optical transparency of (90.2%) and sheet resistance of 36 **Ω**/sq.

The $Glass/Nb_2O_5/SnO_2$stacked layer thin films are used for most of the measurements and the $ITO/Nb_2O_5/SnO_2$ stacked layers thin film will be used for the impedance measurements and current-voltage measurements. The ITO-substrate was necessary for electronic measurements. The $Glass/Nb_2O_5$ and $Glass/SnO_2$ thin films are used for the optical measurements. Thermal evaporation was performed using a VCM 600 thermal vacuum evaporator shown in Fig 3.8 at a vacuum pressure of 10^{-5} mbar.

Fig 3.8. The VCM 600 thermal vacuum evaporation system. Item one is the tungsten boat, item two is substrate holder, item three is the metal plate, and item four is the high-resolution INFICON STM-2 thickness monitor.

To prepare the $Glass/Nb_2O_5/SnO_2$ and $ITO/Nb_2O_5/SnO_2$ stacked layer thin films, ultrasonically cleaned glass substrates and ITO substrates were installed close together on a metal plate (substrate holder) (item 2 Fig 3.8), Then, 0.5 g of high purity Nb_2O_5 powder is situated on the tungsten boat (item1) after which the bell jar is closed. When the vacuum pressure inside the deposition chamber drops and reaches 10^{-5} mbar, the evaporation boat is gradually supplied with current and the movable physical shutter between the evaporation source and the metal plate (item 3) is open two minutes after the vacuum pressure reaches $\sim 10^{-5}$ mbar. The boat is then heated and the Nb_2O_5 powder evaporates and formed on the substrates. After which the shutter is closed again when the desired thicknesses of the thin films is reached. The thickness of the sample is usually monitored by the high-resolution INFICON STM-2 thickness monitor attached to the vacuum system (item 4). The monitor has resolution of 0.037Å. The thickness of the $Glass/Nb_2O_5$ thin films was approximately 100 nm. After the champer was left to cool down to room temperature, $Glass/Nb_2O_5$ and ITO/Nb_2O_5 are taken from the substrate holder. Some of the produced $Glass/Nb_2O_5$ and ITO/Nb_2O_5samples were used as substrates to coat SnO_2.

In this cycle, 0.5 g of high-purity SnO_2 powder is deposited onto a glass substrate, $Glass/Nb_2O_5$ layer and ITO/Nb_2O_5 layer. The thickness of the $Glass/SnO_2$ thin films was 200 nm according to the thickness monitor reading. The Optical images and geometric design of the prepared samples are shown in Fig 3.9.

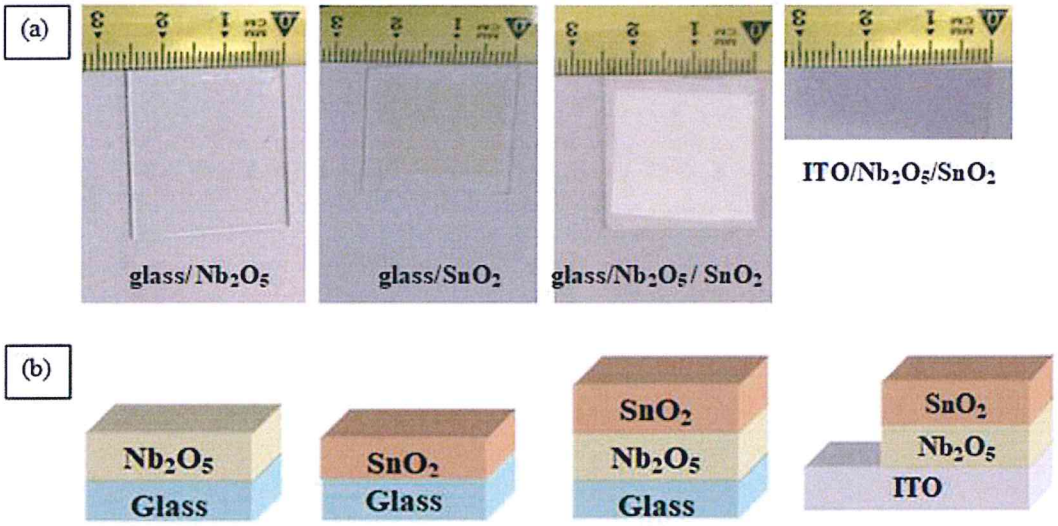

Fig 3.9. (a) The real photography of the films and (b) the geometrical design of the films.

3.3.3: Thickness measurements of the films

After measuring the thickness of the films using the thickness monitor, the thickness measurements of the Glass/Nb_2O_5, Glass/SnO_2 and Glass/Nb_2O_5/SnO_2 thin films were confirmed using profilometer. In this technique, a surface roughness tester - profilometer (model SOLID TR-200 plus) is used to test the correctness of the thickness. Thicknesses of 108, 202, and 330 nm were determined for the Glass/Nb_2O_5, Glass/SnO_2 and Glass/Nb_2O_5/SnO_2 thin films, respectively. The difference in thickness between the measurements of the Inficon STM-2 thickness monitor and those determined by mechanical technique measurement revealed error percentage of about 10% for the Glass/Nb_2O_5 and Glass/SnO_2 thin films, respectively.

Fig 3.10. Optical image of a SOLID NDT portable surface roughness tester - profilometer.

3.4: X-ray diffraction (XRD) Measurements

Both types of bulky and powder samples prepared by laser welding technique, sample produced by the SSR technique at each sintering step and all thin films produced by thermal evaporation technique were subjected to the X-ray diffraction measurements by using Rikago Miniflex 600 X-ray diffractometer shown in Fig 3.11. Miniflex 600 X-ray diffractometer equipped with K_α radiation of a copper anode with average wavelength 1.5405 Å. The X-ray diffractometer records the intensity as a function of the diffraction angle 2θ. The diffraction angle (2θ) starts from 10° to 80°, the scanning speed used is 0.5°/ min and the scanning step is 0.05°. Data were collected by the MiniFlex guidance software connected to the X-ray unit. The obtained XRD data were analyzed using the "TREOR 92" software packages.

Fig 3.11. The optical image of the Miniflex 600 X-ray diffraction.

3.5: Impedance spectroscopy Measurements

The Agilent 421BRF signal generator impedance analyzer shown in Fig 3.12 provides AC signals at room temperature through the samples to measure the impedance of the samples. The impedance analyzer is provided with dielectric test fixture. Impedance (Z), resistance (R), capacitance (C), inductance (L), reactance (X), reflection coefficient (ρ), conductance (G) and other parameters can be measured if the system is treated as an RLC circuit. The impedance consists of two parts, the reactive part and resistive part. The series capacitance (C_s), conductance and impedance spectra in the frequency domain 0.01 - 1.80 GHz are measured by the analyzer and data is read with the help of MATLAB software connected to the system. In order to measure the previous parameters and the current - voltage (I-V) measuments, a silver point contact of area of 3.14×10^{-2} was painted on the surface of each samples; bulky sample prepared by laser welding technique , compact powder prepared by SSR technique and ITO/Nb_2O_5/SnO_2thin film prepared by thermal evaporation technique.

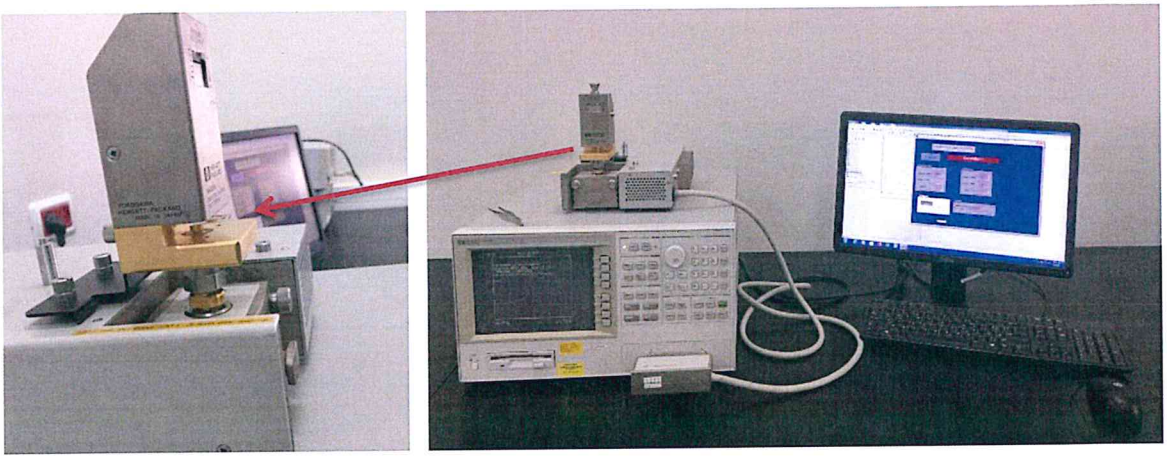

Fig 3.12. The Agilent 421BRF signal generator impedance analyzer spectrometer.

3.6: Current –Voltage (I-V) Measurements

The current - voltage (I-V) measuments were taken at room temperature in order to explore the conductivity behaviour of the bulky sample, ceramic samples and ITO/ Nb_2O_5/SnO_2 thin films which were prepared by laser welding technique , SSR technique and thin film stacking layer technique, respectively. A computerized Keithley 6485 picoammeter and Keithley 235 programmable voltage source connection supported by a software packages constructed on MATLAB which are shown in Fig 3.13 are used to record the Current –Voltage readings. The picomometer has a high sensitivity for measuring currents of less than 0.1 nA. The respective distance between the electrodes of the bulky sample, ceramic sample and ITO/ Nb_2O_5/SnO_2 thin film was measured and found to be 6.30×10^{-2}, 1.34×10^{-1} and 1.00×10^{-4} cm. Dimensions were determined using a digital micrometer.

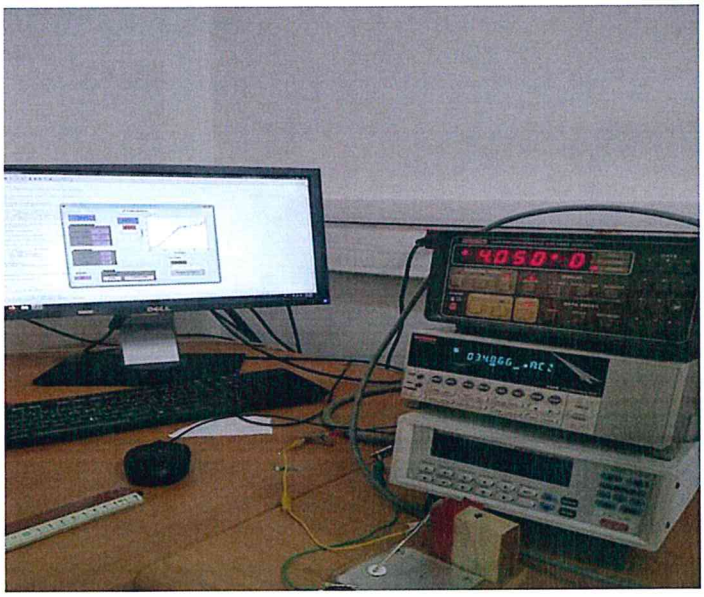

Fig 3.13. Keithley current-voltage characteristics system.

3.7: Optical measurements

$Glass/Nb_2O_5$, $Glass/SnO_2$ and $Glass/Nb_2O_5/SnO_2$ were subjected to optical measurements by thermo-scientific evolution 350 ultra-violet visible light near infrared (UV-VIS-NIR) spectrophotometer equipped with VEE MAX II variable angle reflectometer. The system is illustrated in Fig 3.14. The device uses a xenon (Xe) lamp light. The optical transmittance and reflectance of the incident light on the films were measured at normal incidence with a scanning speed of 1200 nm / min, in the spectral range of 300-1100 nm. During experiments a baseline of 100 % T is used for transmittance measurements and a baseline of 0% T is used with the help of Pike reflectometer to determine the reflectance measurement. The data is collected by a vision software program attached to the system as dispalyed in the figure.

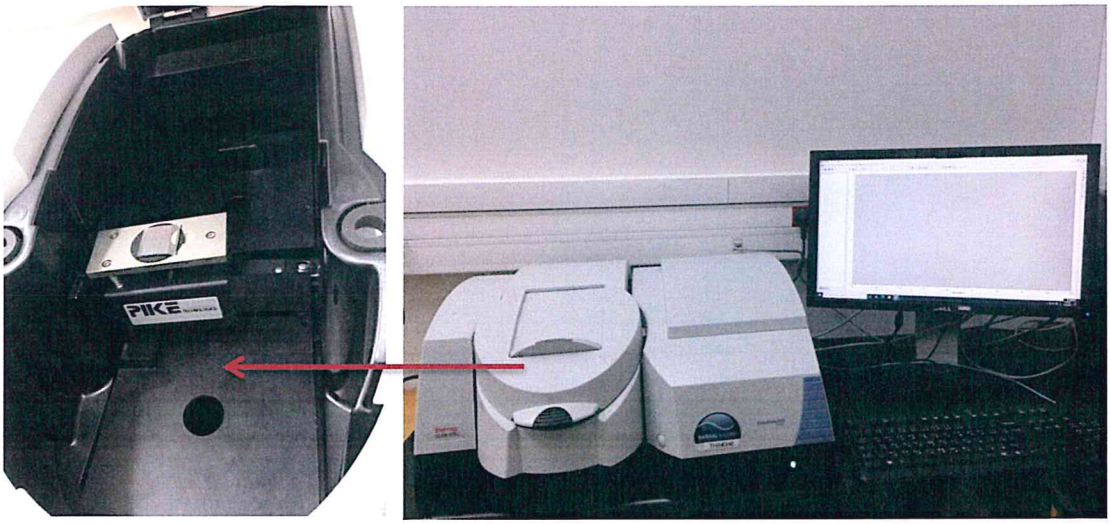

Fig 3.14. Optical image of a UV-VIS-NIR spectrophotometer.

3.7.1: Hot Probe technique

The " hot- probe" techenique is the method used to determine the conductivity types of thin films. The experimental setup is shown in Fig 3.15. During measurement, the thin film is connected by two contacts, a hot soldering iron (hot probe) and a cold probe. Both probes are wired to a Standard Digital Multi-meter (DMM). The hot iron is connected to the positive terminal and the cold iron is connected to the negative terminal. The voltage sign indicates the type of carrier; If the (DMM) reading is positive, the conductivity of semiconductor is n-type while the p-type semiconductor gives a negative reading. At the hot probe, the thermal energy of the majority carriers is higher than at the cold probe, so the carriers diffuse from the hot probe to the cold probe leaving uncompensated ions; this will produce a current or (voltage) difference. For n- type, the majority carriers are electrons; the area around the hot probe (the positive lead) becomes positive charged. The majority carriers for p- type material are holes, the polarity of the induced voltage is

reversed. In our experiment, a negative voltage was read on the multimeter when the probes were applied to the Glass/Nb_2O_5 and Glass/SnO_2 thin films, indicating the p-type materials.

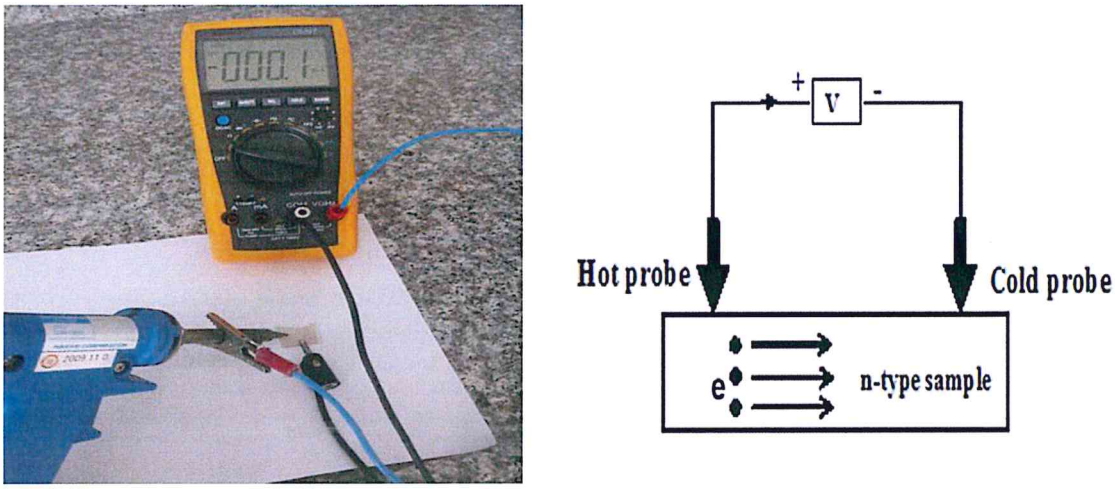

Fig 3.15. The experiment set-up for hot-probe technique.

Chapter Four

Results and Discussions

4.1: Structural analysis

4.1.1: Laser welding technique

In the laser welding (LW) technique, two equal quantities of high purity of Nb_2O_5 (99.9989%) and SnO_2(99.99%) were exposed to laser light and two types of $SnNb_2O_6$ were obtained. One in powder form and the other is a bulky alloy. The XRD patterns for Nb_2O_5 pressed powders, SnO_2 pressed powders and $SnNb_2O_6$: pressed powders and bulky samples are shown in Fig 4.1.

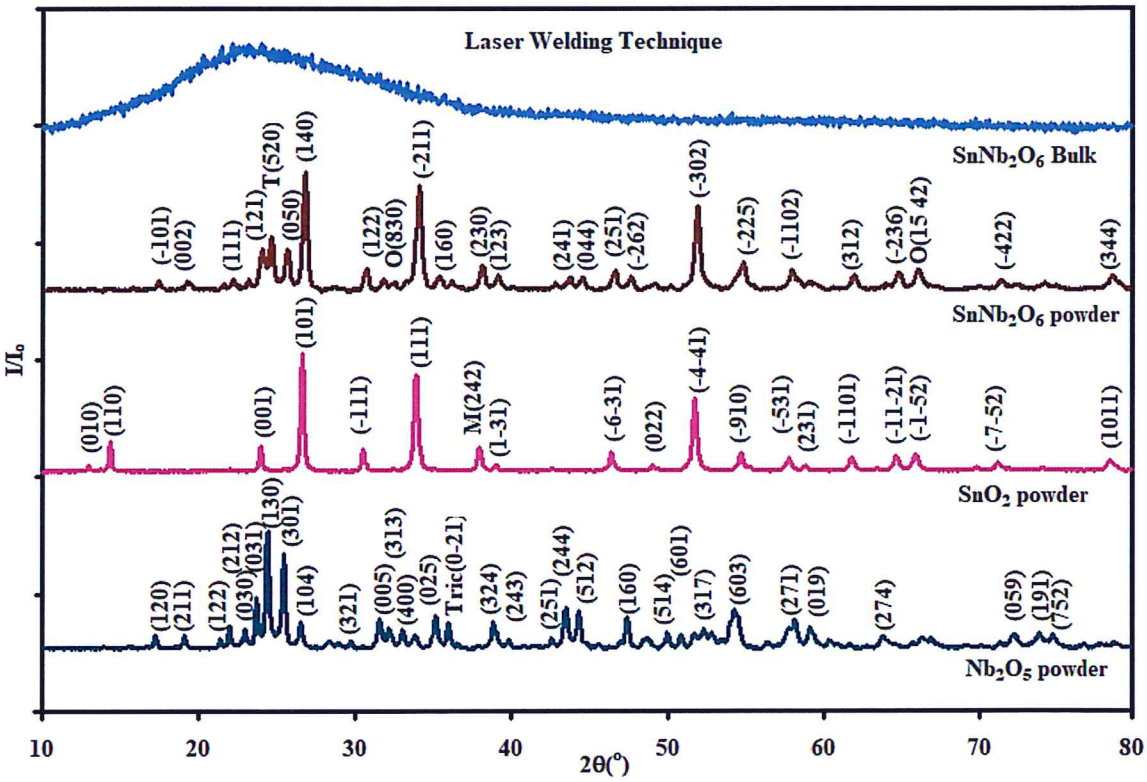

Fig 4.1.The X-ray diffraction patterns of raw material Nb_2O_5 pressed powders and SnO_2 pressed powders, and $SnNb_2O_6$ with both types; pressed powders and bulky samples prepared by laser welding technique.

As can be seen from Fig 4.1, the polycrystalline nature of Nb_2O_5, SnO_2 and $SnNb_2O_6$ pressed powders were generally observed. The amorphous nature of $SnNb_2O_6$ bulky samples is evidenced by the absence of intense peaks of the recorded XRD spectra. The observed sharp patterns were analyzed with the help of "TREOR 92" and "Crystdiff" software packages. The "TREOR 92" software packages can be used in two ways to reveal solutions. The first method is to enter the observed 2θ and intensity values of the observed XRD peaks, then suggest a crystal structure. The software determines the planes Miller indices of the sharp patterns (hkl) (plane orientation of the crystal) and the lattice parameters. The appropriate crystal structure is manually determined by comparing the difference ($\Delta(2\theta)$) between the experimentally observed and theoretically calculated 2θ for the sharp peaks. The most acceptable solution is the one which display least $\Delta(2\theta)$ values. For our calculations we accepted $\Delta(2\theta)$ values less than $0.1°$. In other words, if $\Delta(2\theta)$ is larger than $0.1°$ then the crystal structure is regarded as not appropriate for the observed reflection peak. The second method is achieved by applying the Bragg lattice of the unit cell, space groups and the lattice parameters for a selected crystal structure. Here, the lattice parameters are taken from literature data. The software packages give the expected reflection peaks (diffraction angle of the peaks, Miller indices and the intensity of the peaks). By this method, the result from the literature data is compared to the observed data.

For the Nb_2O_5 spectrum, comparing the literature data (monoclinic [48], orthorhombic [49,50], tetragonal [50]) with the observed experimental data which are reproduced with the help of "Crystdiff " software packages did not show a relation between our observation and published data. The literary sharp patterns did not match all the observed sharp patterns

observed in our experiment. It may be speculated that the experimental structure is more complex and may contain more than one structural phases. Therefore, "TREOR 92" was employed to determine the crystal structure of Nb_2O_5 and related lattice parameters. The X-ray patterns of Nb_2O_5 displayed 41 peaks and the most intensive peak is centered at diffraction angle 2θ of 24.4° displaying an intensity of 9047 counts/s. The results obtained from "TREOR 92" are shown in Table 4.1. Tabulated data show the percentage difference between 2θ of observed and calculated peaks for all possible crystal structures. It also displays the experimental values of 2θ and the respective peak intensities.

In order to make the decision to determine the appropriate crystal structure from the tabular data taken from the " TREOR 92" software packages, Since 10% or less percentage of diffraction angle difference $(\Delta(2\theta))\%$ is accepted to determine the crystal structure, we also take into consideration: the number of zeros of percentage for the angle difference value, the percentage of diffraction angle difference at the most intensive peak in particular and at other peaks in general. Moreover, the number of observed peaks of the least percentage of error in each structure.

From Table (4.1), the ranges of the percentage of diffraction angle difference in each crystal structure are (0- 43) % for triclinic, (0-22) % for orthorhombic, (0-21) % for monoclinic, (0-24) % for tetragonal, (0-40) % for trigonal and hexagonal and (0-46) % for cubic structure. By comparing the ranges keeping in mind the previously mentioned points, hexagonal and cubic structures are excluded, with the fewest zeros, high percentage of error and least number of observed peaks. The Nb_2O_5 powder structure is completely orthorhombic with lattice parameters of a = 10.836, b = 11.666, and c = 14.168 Å. One diffraction peak centered at 35.95 ° is triclinic. The Miller indices (hkl) and related structure

of each peak of the Nb_2O_5 pressed powders spectrum which appears in Fig 4.1 are indexed using the results obtained by "TREOR 92" software packages.

On the other hand, for SnO_2, the " Crystdiff " software packages which were used to compare the experimental results with the literature data (orthorhombic [51] and tetragonal [52]), show a crystal structure closer to tetragonal than orthorhombic. Still the XRD patterns of SnO_2 display 10 undetermined peaks. The results obtained by "TREOR 92" software packages for 23 observed peaks were tabulated (Table 4.2) to determine the structure of the SnO_2 powder. The most intensive peak is centered at 26.6° at an intensity of 15778 counts/s. After careful analysis, the cubic, hexagonal, trigonal and tetragonal structures were excluded from the expected structure solution. They have a high percentage of error. Assuming less difference between the observed and calculated peaks, there is more than one phase in the crystal structure. The triclinic structure is represented as the dominant structural phase in which there is no error in the five highest peaks. Orthorhombic structure is represented as a secondary structural phase with a lower value of difference percentages when compared to monoclinic structure. Additionally, monoclinic was represented as a minor phase. If 0.1° of the diffraction angle difference is considered. The crystal structure is completely triclinic, except for one peak at 37.95 ° that belongs to monoclinic structure. The lattice parameters for this structure are a = 16.6407, b = 7.4674, and c = 4.3576 Å. The reflection planes and related structural phases for each peak of the SnO_2 XRD patterns are indexed and shown in Fig 4.1. The indexing was carried out with the help of "TREOR 92" software packages.

Table 4.1: Possible crystal structures of their percentage of diffraction angle difference value of 41 sharp peaks with their intensity for the Nb_2O_5 pellets, which was investigated by "TREOR 92" software packages.

2θ	I (c/s)	I/I_o	Triclinic%	Ortho.%	Monoclinic%	Tetragonal%	Trigonal%	Hexagonal%	Cubic%
17.25	1438	0.16	0	0	0	0	0	0	0
19.10	1509	0.17	0	0	0	0	0	0	18.9
21.35	1393	0.15	0	0	0	12.9	4.2	4.2	-
22.00	2222	0.25	0	0.5	0	4.8	2.4	2.4	13.0
22.95	2084	0.23	0	10.1	10.5	5.3	1.7	1.7	26.4
23.70	4368	0.48	0	0.6	3.9	5.7	26.3	26.3	-
24.40	9047	1.00	-	10.3	4.7	8.7	39.4	39.4	8.9
25.45	7448	0.82	0.6	2.4	5.0	0.9	2.1	2.1	25.4
26.50	2661	0.29	26.3	4.8	50.0	13.9	28.0	28.0	36.8
29.00	1235	0.14	5.7	5.2	14.9	0.2	9.7	9.7	6.7
29.75	1287	0.14	43.3	0.8	10.3	21.5	36.0	36.0	-
31.55	2969	0.33	13.5	0.3	15.5	12.6	7.2	7.2	42.7
32.15	2342	0.26	4.6	5.1	3.2	4.6	15.2	15.2	4.4
33.00	2220	0.25	2.4	3.7	17.1	0.8	10.3	10.3	6.3
33.85	1730	0.19	11.1	0.9	3.4	0.9	0.4	0.4	14.6
35.15	3099	0.34	12.4	3.1	15.4	2.5	7.1	7.1	24.3
35.95	2547	0.28	2.6	21.7	15.4	16.4	4.7	4.7	15.2
36.60	1020	0.11	24.9	2.5	2.6	6.9	0.4	0.4	7.0
38.80	2526	0.28	4.2	2.3	1.9	4.2	4.2	4.2	38.6
39.90	1197	0.13	4.6	2.6	4.3	8.2	9.1	9.1	9.5
42.65	1277	0.14	2.4	1.6	13.7	5.8	5.8	5.8	30.6
43.50	3505	0.39	1.0	1.0	1.0	5.2	7.8	7.8	39.6
44.35	3279	0.36	6.2	0.6	6.8	8.3	8.4	8.4	24.2
47.45	3069	0.34	15.3	1.6	2.9	3.3	15.5	15.5	0.7
48.75	1618	0.18	23.1	0.4	13.0	7.5	31.2	31.2	9.1
49.95	1008	0.11	22.4	4.6	10.4	5.7	1.2	1.2	24.6
50.90	1711	0.19	29.4	2.8	21.4	1.1	2.5	2.5	3.6
51.75	1952	0.22	17.7	2.1	18.7	10.2	23.0	23.0	22.5
52.40	2292	0.25	8.6	3.8	1.5	5.2	0.8	0.8	21.9
54.35	3616	0.40	10.1	1.2	0.3	0.8	1.8	1.8	23.7
56.55	1197	0.13	6.6	0.6	1.1	15.6	16.8	16.8	6.9
58.20	2691	0.30	5.4	3.4	2.6	23.8	1.7	1.7	25.2
59.20	2147	0.24	6.5	2.7	0.9	3.3	25.8	25.8	14.5
60.55	1232	0.14	12.1	4.6	0.6	3.1	1.9	1.9	29.1
63.95	1447	0.16	3.6	8.8	7.0	6.4	2.3	2.3	19.7
66.55	1257	0.14	3.5	5.0	2.0	2.8	4.2	4.2	4.3
66.95	1315	0.15	19.9	2.0	2.3	14.4	4.6	4.6	20.3
72.35	1496	0.17	5.1	0	0.5	0.1	8.0	8.0	24.7
73.85	1667	0.18	9.5	2.3	3.5	5.3	5.9	5.9	12.9
74.75	1528	0.17	1.3	1.2	14.7	0.6	22.3	22.3	4.2
79.05	1036	0.11	0.8	0.7	9.3	2.5	1.6	1.6	2.4

Table 4.2: Possible crystal structures with their percentage of diffraction angle difference values of 23 sharp peaks with their intensity for the SnO_2 pellets, which was investigated by "TREOR 92" software packages.

2θ	I (c/s)	I/I_o	Triclinic%	Ortho.%	Monoclinic%	Tetragonal%	Trigonal%	Hexagonal%	Cubic%
13.00	1370	0.09	0	0	0	0	0	0	0
14.40	4432	0.28	0	0	0	0	0	0	62.2
23.95	4375	0.28	0	0	0	15.8	16.4	5.5	9.4
26.60	15778	1.00	0	6.7	0	5.6	2.1	42.9	42.9
30.50	3713	0.24	0	3.6	1.0	1.3	50.4	13.2	19.0
33.85	12751	0.81	0	8.2	8.2	8.2	15.9	14.3	14.0
37.95	3554	0.23	12.8	7.6	23.6	5.8	5.8	0.7	19.8
39.05	1118	0.07	8.8	4.4	2.3	2.2	0	16.7	11.6
42.75	653	0.04	3.5	2.7	20.0	30.4	8.4	19.3	64.7
46.40	2760	0.17	0.2	0.1	3.7	0.5	5.3	23.4	22.4
49.10	1053	0.07	6.5	1.3	6.5	13.2	14.3	2.4	26.8
51.75	9444	0.60	0.5	3.6	4.5	16.5	31.8	9.7	25.8
54.70	2673	0.17	0.4	4.1	8.7	3.7	1.7	36.4	24.7
57.80	1923	0.12	0.3	3.1	2.0	0	8.1	9.3	39.3
58.95	857	0.05	10.0	1.6	1.1	1.8	18.4	3.7	18.4
61.80	2064	0.13	4.5	1.2	1.3	5.5	5.5	5.5	14.5
63.65	563	0.04	2.0	0.2	8.9	8.9	2.9	12.4	5.3
64.70	2153	0.14	0.9	0.2	0.3	8.8	10.1	5.4	1.5
65.90	2413	0.15	4.6	5.0	0.9	1.0	8.5	20.7	13.7
69.90	604	0.04	1.0	1.2	0.4	5.7	1.8	1.0	9.1
71.25	1186	0.08	0	2.9	2.6	3.8	21.3	16.3	29.6
74.15	521	0.03	5.6	0.8	0.2	6.2	6.8	2.5	4.2
80.06	1681	0.11	1.3	0.1	0.3	2.7	10.0	2.4	0.7

The sharp XRD patterns of $SnNb_2O_6$ were compared with the literature data which reported Monoclinic, orthorhombic and tetragonal structures [53]. Production of the XRD patterns was carried out with using "Crystdiff" software packages. The literary patterns did not match all the observed patterns. It means that $SnNb_2O_6$ preferred another crystal structure when prepared by LW technique. The "TREOR 92" software packages were used to determine the crystal structure of $SnNb_2O_6$ pressed powders prepared by the laser method. The results of 37 observed peaks are presented in Table 4.3. The ranges of percentage difference for the seven crystal structure are, (0-47) % for triclinic, (0-10) % for orthorhombic except one $\Delta(2\theta)$ value with an error 39%, (0-22) % for monoclinic, (0-31) % for tetragonal, (0-37) % for trigonal and hexagonal and (0-45) % for cubic structure. The cubic and triclinic structures were excluded from the solution due to the large range of percentage of error and the least number of observed peaks with the least percentage of error. However, $SnNb_2O_6$ pressed powder mostly shows a monoclinic structure with lattice parameters of a = 5.3352, b = 17.4108, and c = 9.4486 Å. The peaks centered at 24.6° and 32.55° and 66.05° exceeding 10% error can be assigned to the tetragonal and orthorhombic structures, respectively. The reflection planes and related structural phases for each peak of the $SnNb_2O_6$ XRD patterns are indexed and shown in Fig 4.1.

Table 4.3: Possible crystal structures of their percentage of diffraction angle difference value of 37 sharp peaks of their intensity for $SnNb_2O_6$ pressed powders prepared by LW technique, which was investigated by "TREOR 92" software packages.

2θ	I (c/s)	I/I_o	Triclinic%	Ortho.%	Monoclinic%	Tetragonal%	Trigonal%	Hexagonal%	Cubic%
17.50	1060	0.16	0	0	0	0	0	0	14.2
19.35	1110	0.16	0	0	0	0	0	0	104
21.65	1073	0.16	0	0	0	13.1	0.6	0.6	0
22.25	1218	0.18	0	3.5	0	1	4.1	4.1	-
23.20	1286	0.19	0	5.4	6.3	10.6	6.8	6.8	36.4
24.05	2880	0.42	0	1.2	8.6	3.8	13.3	13.3	8.3
24.60	3561	0.53	31	39	13.1	3.4	27.8	27.8	45
25.65	2926	0.43	46.6	10.4	9.1	14.4	0	0	44
26.75	6780	1.00	13.4	5.5	1.3	4.1	37.3	37.3	34.4
30.70	1829	0.27	4	0.8	6.2	12	5.1	5.1	10.6
31.80	1292	0.19	1.2	0.1	5.9	31.1	-	-	12.8
32.55	1071	0.16	-	1.1	21.8	1.8	14.1	14.1	3.3
34.05	5904	0.87	8.8	1.8	5.2	3.7	0.8	0.8	10.1
35.45	1231	0.18	2.4	2.4	1.7	2.4	2.4	2.4	27
36.15	990	0.15	19.2	0.7	2.9	10.6	2.7	2.7	33.2
38.10	1718	0.25	8.6	2.1	6.2	2.9	4.8	4.8	13.3
39.10	1230	0.18	18.1	1.8	4.7	17.9	18.1	18.1	30.4
40.10	584	0.09	4.3	0.4	2.8	2.4	3.3	3.3	0.6
42.85	732	0.11	5.3	2.3	1.3	1	0.8	0.8	3
43.80	999	0.15	14.6	7.5	0.5	2.2	15.6	15.6	32.4
44.60	1026	0.15	5.8	3.7	5	19.8	24.2	24.2	16.7
46.65	1431	0.21	5.6	4.5	1.1	2	6.7	6.7	0.1
47.65	1169	0.17	5.4	3.3	2.3	0.1	7.9	7.9	22.2
49.30	779	0.11	5	2.4	0.6	3.2	3.8	3.8	22.8
50.25	745	0.11	19.4	3.1	5.9	3.4	2.4	2.4	0
51.95	4751	0.70	24.9	10.4	9.6	5.7	3.7	3.7	3.1
54.85	1832	0.27	2.7	1.9	2	10.2	2.9	2.9	7.1
57.95	1419	0.21	13.3	1.7	9.4	3.8	2.2	2.2	46.6
59.25	787	0.12	5.4	1.8	6.3	5.5	0.7	0.7	18.2
62.05	1125	0.17	36.2	0.8	3.4	6.1	13.2	13.2	11.1
64.10	666	0.10	25.7	7.1	0.4	10.6	5	5	7.4
64.85	1267	0.19	5.4	3.7	1.3	9.8	6.7	6.7	17.8
66.05	1399	0.21	0.9	1.2	22.1	6	2.7	2.7	10.4
71.50	791	0.12	1.9	10.2	6.5	3.6	3.7	3.7	42.7
72.60	459	0.07	3.7	5.5	4.6	7	0.1	0.1	20.1
74.20	708	0.10	0.4	0	2.4	1.9	2.3	2.3	7.4
78.80	1114	0.16	6.4	2	2.2	0.2	4.7	4.7	36.6

The phase weights for SnO_2 and Nb_2O_5 pellets and for $SnNb_2O_6$ pellet prepared by the LW technique are shown in Table 4.4. As can be seen from the values of the Table, the phase weights of the bulky sample differ from the two raw materials SnO_2 and Nb_2O_5.

Table 4.4: Phase weight for crystal structures of $Nb_2O_5$and SnO_2 pellets and $SnNb_2O_6$ pellets prepared by laser welding.

Sample	Phase weight % of possible crystal structural			
	Triclinic	Ortho.	Monoclinic	Tetragonal
Nb_2O_5	2.3	97.7	-	-
SnO_2	95.3	-	4.7	-
$SnNb_2O_6$ powder	-	4.3	90.0	5.8

Comparison of the sharp patterns of Nb_2O_5, SnO_2 raw pellets and $SnNb_2O_6$ pellets prepared by laser welding technique reveals that $SnNb_2O_6$ is an alloy produced from the laser welding process. The crystal structure, lattice parameters and structural parameters of $SnNb_2O_6$ prepared by laser welding differ from the structure of the two raw materials as shown in Table 4.7.

4.1.2: Solid state reaction technique

Mixed equal quantities of SnO_2 and Nb_2O_5 powders were sintered to produce $SnNb_2O_6$ ceramics. The thermal sintering cycle was performed in the range of $1000 - 1300°C$ for different periods of sintering times. The sintering cycles started with T = 1000 °C for 2 hrs, 1100 °C, 1200 °C and 1300 °C for 3 hrs and 1300 °C for 6 hrs. Fig.4.2 shows the resulting XRD patterns for each sintering cycle. In general, as the temperature increases, some peaks completely disappear or become less intense.

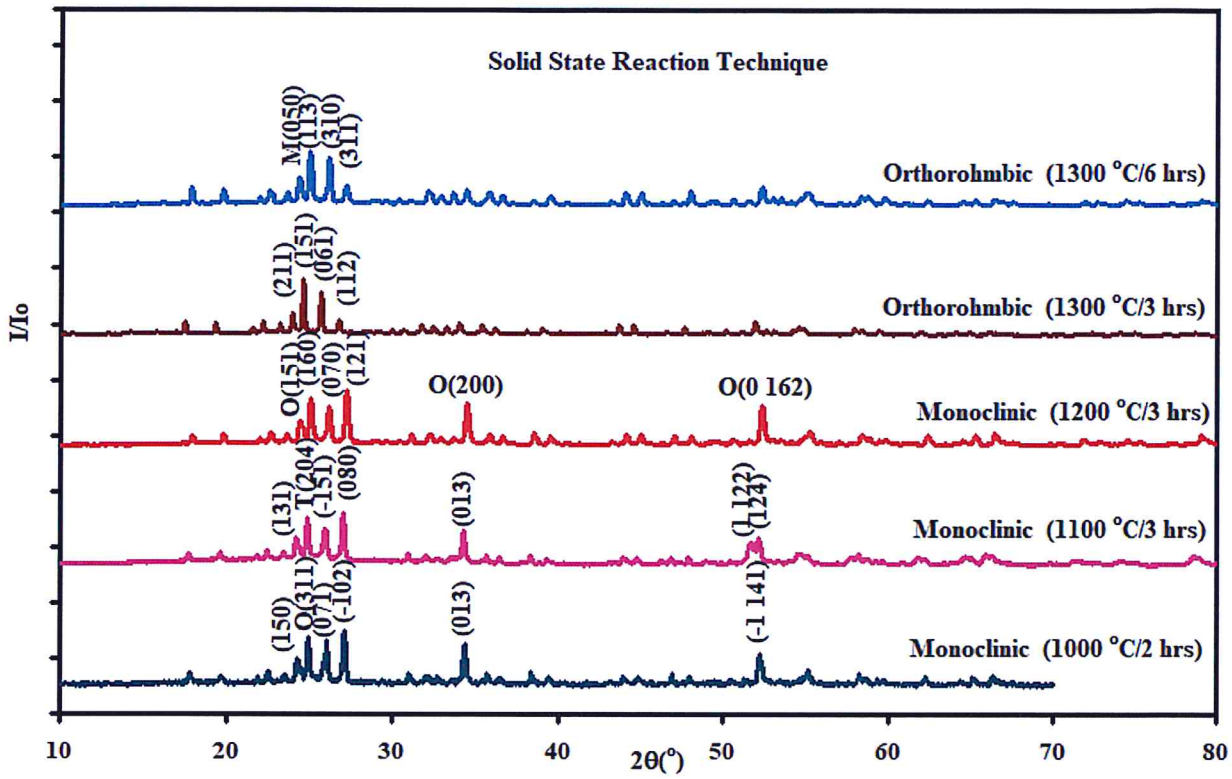

Fig 4.2. The X-ray diffraction patterns of $SnNb_2O_6$ ceramics centered at various temperature in the range of $1000°C - 1300°C$ at different sintering times.

The maximum peak exhibited a significant shift in the sintering step of 1300°C/3 hrs or higher. Moreover, a significant change occurred in the intensity of the peaks, with peaks intensities being the largest compared to the other sintering stages. XRD patterns were analyzed for $SnNb_2O_6$ powder that was sintered at 1000°C /2 hrs and shown in Fig 4.2 with the help of the "TREOR 92" software packages. The results of percentage error obtained from the software for all possible structural phases for the 30 observed peaks are tabulated in Table 4.5. The major peaks, from highest to lowest intensity, of the spectrum are centered at 27.15°, 24.95°, 26.05°, 34.4°, 52.25° and 24.25°, respectively. When 0.1° of the diffraction angle difference are accepted ,the crystal structure of the powder is completely

monoclinic, except for the second maximum peak at 24.95° which belongs to the orthorhombic structure. The structural phase and Miller indices for each of the main reflection peaks of $SnNb_2O_6$ ceramic sintered at 1000°C / 2 hrs are shown in Fig 4.2. XRD analysis of the compacted powder sintered at 1100°C / 3 hrs showed a monoclinic structure as the dominant structural phase, with the most intensive peak of the spectrum centered at 27.05°. The tetragonal phase is represented as a minor structural phases. The crystal structure of the sample sintered at 1100°C/ 3 hrs is still monoclinic as that at 1000°C / 2 hrs but with different values of lattice parameters and different secondary phase. The spectrum of the pressed powder sintered at 1200°C / 3 hrs shows a most intensive peak centered at 27.25°. XRD analysis revealed that the appropriate dominant structure was still monoclinic with new cell parameters and the orthorhombic structure returned as a secondary structural phase. Increasing the sintering temperature to 1300°C / 3 hrs affects the crystal structure and resulted in single phase formation. Namely, the main reflection peak shifted to 24.6° and the main crystal structure displayed transition from monoclinic structural phase with a lattice parameters of a = 8.8035, b = 23.827, and c = 4.9944 Å to an orthorhombic structural phase with a cell units of a = 8.7659, b = 23.729 and c = 7.288 Å. In the final step of the sintering process which was carried out at 1300°C for a period of 6 hrs, the most intensive peak is centered at 25.00° . XRD analysis revealed the orthorhombic structure with new lattice parameters of a = 10.511, b = 14.765, and c = 11.728 Å is still dominant as the main structural phase. The monoclinic phase appears as a secondary structural phase. The reflection planes of the most intensive peaks of each spectrum in the sintering process are displayed in Fig 4.2.

Table 4.5: Possible crystal structures with their percentage of diffraction angle difference values of 30 sharp peaks with their intensity for $SnNb_2O_6$ ceramic sintered at 1000°C for 2hrs, which was investigated by "TREOR 92" software packages.

2θ	I (c/s)	I/I_o	Triclinic%	Ortho.%	Monoclinic%	Tetragonal%	Trigonal%	Hexagonal%	Cubic%
17.85	53	0.23	0	0	0	0	0	0	0
19.75	42	0.18	0	0	0	0	0	0	89.0
21.95	38	0.17	0	0	0	38.0	25.1	25.1	4.3
22.60	60	0.26	0	11.5	0	5.4	8.5	8.5	-
23.60	47	0.21	0	0.2	1.9	2.9	8.6	8.6	49.3
24.25	114	0.50	0	9.5	2.5	0.6	37.1	37.1	0.2
24.95	199	0.87	50.1	2.8	19.5	10.8	21.7	21.7	39.8
26.05	185	0.81	14.1	4.2	2.0	7.2	17.0	17.0	35.1
27.15	229	1.00	8.2	20.1	7.6	1.2	23.6	23.6	26.7
31.00	53	0.23	40.8	6.7	8.8	6.4	2.6	2.6	17.5
32.20	43	0.19	28.1	0.5	0.8	2.3	13.9	13.9	14.8
32.70	37	0.16	2.2	4.4	5.7	3.1	21.7	21.7	20.8
34.40	176	0.77	7.2	0.8	4.4	44.3	2.4	2.4	16.4
35.70	54	0.24	19.1	12.2	0.3	3.1	7.1	7.1	45.3
36.55	35	0.15	18.6	1.1	6.5	13.1	1.0	1.0	37.5
38.40	58	0.25	7.2	5.5	6.4	1.3	9.6	9.6	2.9
39.45	43	0.19	18.7	0.3	0.2	1.0	7.5	7.5	43.5
41.80	20	0.09	6.8	3.8	2.7	4.7	7.1	7.1	19.0
44.05	36	0.16	1.4	1.7	2.4	7.5	15.2	15.2	3.8
44.90	42	0.18	0.6	10.0	0.2	4.0	9.6	9.6	23.0
46.90	51	0.22	12.6	0.2	0.7	5.9	1.4	1.4	32.8
48.00	43	0.19	1.8	1.7	5.9	2.9	25.6	25.6	14.9
52.25	133	0.58	2.9	0.4	0.1	11.0	8.9	8.9	19.5
55.15	69	0.30	14.0	1.4	7.3	6.3	5.0	5.0	23.4
58.25	55	0.24	15.9	2.4	5.7	5.7	12.2	12.2	2.9
59.70	29	0.13	4.4	7.3	2.8	10.1	3.8	3.8	12.9
62.25	40	0.17	6.3	2.8	1.3	5.6	5.6	5.6	20.4
64.35	29	0.13	0.3	0.1	0.9	5.8	32.6	32.6	35.1
65.05	39	0.17	8.7	0.6	1.8	10.7	3.3	3.3	3.3
66.35	45	0.20	3.8	10.6	1.7	5.1	9.5	9.5	17.9

As shown in Fig 4.3(a) which represents the displacement of the main reflection peak of the spectrum of the first three sintering steps, the three samples have a monoclinic structure as the main structural phase. An increase in temperature from 1000 ° C to 1100 ° C causes a

sharp increase in the X-ray diffraction intensity. Particularly, the major peak that appears at a diffraction angle of $2\theta = 27.15°$ and is oriented in the $(\bar{1}02)$ direction with an intensity value of 229 counts/s at 1000°C shifted to the left at $2\theta = 27.05°$ and oriented in (080) direction with an intensity value of 8611 counts/s at 1100°C. When the sintering temperature is raised at 1200°C, the most intensive peak shifts to the right at a diffraction angle of $2\theta = 27.25°$ with a plane orientation (121) and with a slight decrease in the intensity value 5829 counts/s.

Increasing the sintering temperature to 1300°C/3 hrs resulted in transition in the crystalline structural phase from monoclinic to orthorhombic phase with no secondary phases. Fig 4.3(b) shows the deviation of the most intensive peak of the samples sintered at 1300°C /3 hrs and 1300°C /6 hrs. The most intensive peak centered at 24.6° shifted to the right as the sintering temperature increased, and the intensity values decreased from 38652 counts/s to 7439 counts/s when changing the sintering steps from1300°C/3 hrs and 1300°C/6 hrs, respectively. Moreover, XRD patterns of 1300°C/3hrs and 1300°C/6hrs displayed the same dominant structural phase (orthorhombic) with different plane orientations which are (151) and (113) for the most intensive peaks, respectively.

The sintering process causes a decrease in the intensity of X- ray diffraction and leads to a shift toward larger angles in the peak position and broadening between the two sintering steps at 1100°C/3 hrs and 1200°C /3 hrs as shown in Fig 4.3(a). Moreover, the sintering process causes a sharp fall in the intensity of X- ray diffraction and leads to a shift in the position of the peak and broadening between the sintering steps at 1300°C/ 3 hrs and 1300°C/6 hrs as shown in Fig 4.3(b), indicated the formation of non-uniform deformation or plastic deformations [54].

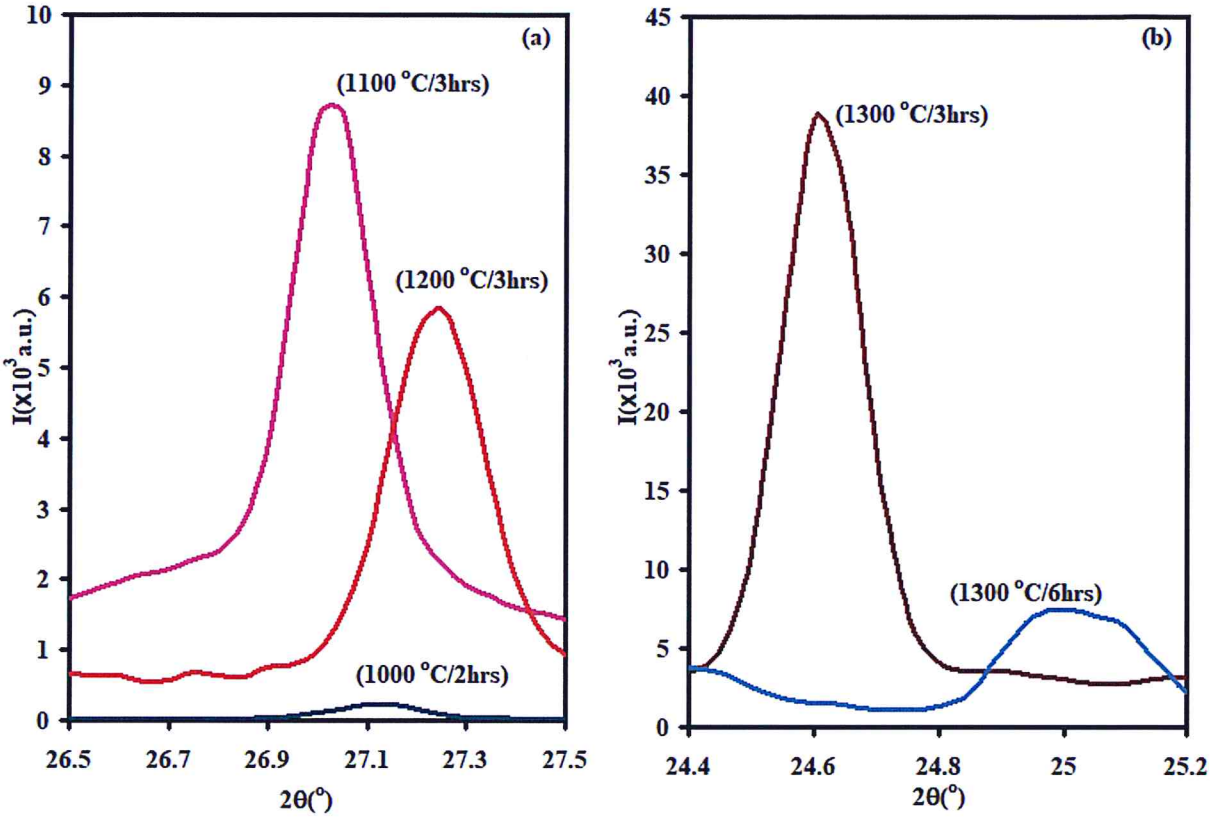

Fig 4.3. Enlargement of the maximum peak as a function of sintering temperature and sintering time of (a) 1000°C/2 hrs , 1100°C/3 hrs and 1200°C/3 hrs and (b) at 1300°C/3 hrs and 1300°C/6 hrs .

To investigate the changes in the crystal structure and the phase development of the sample prepared by SSR technique after heat treatment, the percentage of the phases for the sintered pressed powder were determined at each step of the sintering process. The results are shown in Table 4.6. The phase weights of the $SnNb_2O_6$ ceramic sample differ from their crude components which are SnO_2 and Nb_2O_5. The sintering process clearly affected the phase weight of the crystal structures. The Table 4.6 indicates that the single phase formation is highly dependent on temperature and heating times, since sintering at high temperature of 1300°C/3 hrs was required to obtain a single structural phase.

Table 4.6: Phase weight for crystal structures of $SnNb_2O_6$ ceramic at each step of the sintering process

sintering stage	Phase weight % of possible crystal structural		
	Orthorhombic	Monoclinic	Tetragonal
1000°C/2 hrs	17.4	82.6	-
1100°C/3 hrs	-	83.6	16.4
1200°C/3 hrs	28.6	71.4	-
1300°C/3 hrs	100	-	-
1300°C/6 hrs	85.3	14.7	-

The structural parameters presented by crystallite size (D), microstrain (ε), dislocation density (δ) and stacking faults percentages (SF %) are calculated according to the previously mentioned equations (2.1), (2.2), (2.3) and (2.4) from the most intensive peak position and broadening for raw powders $Nb_2O_5$and SnO_2, $SnNb_2O_6$ prepared by laser LW technique and $SnNb_2O_6$ prepared by SSR technique. In addition, the values of the lattice parameters obtained from the "TREOR 92" software packages for the dominant structures are presented for each sample. The results are shown in Table 4.7.

At this stage, comparison between SSR method (T = 1300°C/6 hrs) and laser method is sufficient. SSR method achieved larger values for crystalline sizes, lower values for microstrains and stacking fault percentages. The values of the crystallite sizes are consistent with those reported in literature data [55]. Lesser defect density is achieved by the SSR method.

The structural parameters of the sintered samples were also examined at each sintering temperature and heating time. As is evident from the table values of the sintering process, the crystal structural parameters of the sintered samples depend on the sintering temperature

and the heating time. In accordance with the table, raising the sintering temperature is associated with crystallite growth in the sintering temperature range of 1000 – 1300°C. Increasing the sintering time caused shrinkage in the crystallite sizes. This increase in grain size with an increase in the sintering temperature from 1000°C to 1300°C at a constant time is due to the enhancement of grain growth and the decrease in the number and sizes of the pores with an increase in the sintering temperature. The presence of larger grains is associated with the growth of smaller grains or they may be caused by clumping of smaller grains [56], which leads to the enhancement of crystallinity [57]. On the other hand, changes in the strain as a result of sintering procedure are assigned to the increase in stress. The stress increases due to increase in internal energy which causes further deformation defects to be observed [58] and an increase in the constraint stress between the grains [59].

Table 4.7: Lattice parameters and structural parameters for SnO_2 , Nb_2O_5 and $SnNb_2O_6$ bulk prepared by LW. In addition, for $SnNb_2O_6$ ceramic sample at each step of sintering process.

Sample	2θ (°)	I (c/s)	a (Å)	b (Å)	c (Å)	D (nm)	ε ($X10^{-3}$)	SF%	δ $X10^{12}$(line/cm^2)
Nb_2O_5	24.40	9047	10.836	11.666	14.168	42.46	4.04	0.19	0.13
SnO_2	26.60	15778	16.641	7.467	4.358	42.65	3.69	0.18	0.08
$SnNb_2O_6$ powder	26.75	6780	5.335	17.411	9.449	24.38	6.42	0.32	0.74
$SnNb_2O_6$ ceramic									
1000°C/2 hrs	27.15	229	5.087	26.589	7.914	24.40	6.32	0.31	0.76
1100°C/3 hrs	27.05	8611	5.105	26.412	7.951	42.69	3.63	0.18	0.25
1200°C/3 hrs	27.25	5829	8.804	23.827	4.994	42.71	3.60	0.18	0.14
1300°C/3 hrs	24.60	38652	8.766	23.729	7.288	56.64	3.00	0.14	0.09
1300°C/6 hrs	25.00	7439	10.511	14.765	11.728	34.01	4.92	0.23	0.21

4.1.3: Thermal evaporation technique

When using a thin film stacking layers technique to prepare two stacked layers of Nb_2O_5 and SnO_2. Nb_2O_5/SnO_2 films were evaporated onto glass substrates. The XRD pattern reveals the amorphous nature of thin film structure of Glass/Nb_2O_5, Glass/SnO_2, and Glass/Nb_2O_5/SnO_2 grown on glass substrate, where no intensive peaks appear in the recorded XRD spectra as shown in the Fig 4.4.

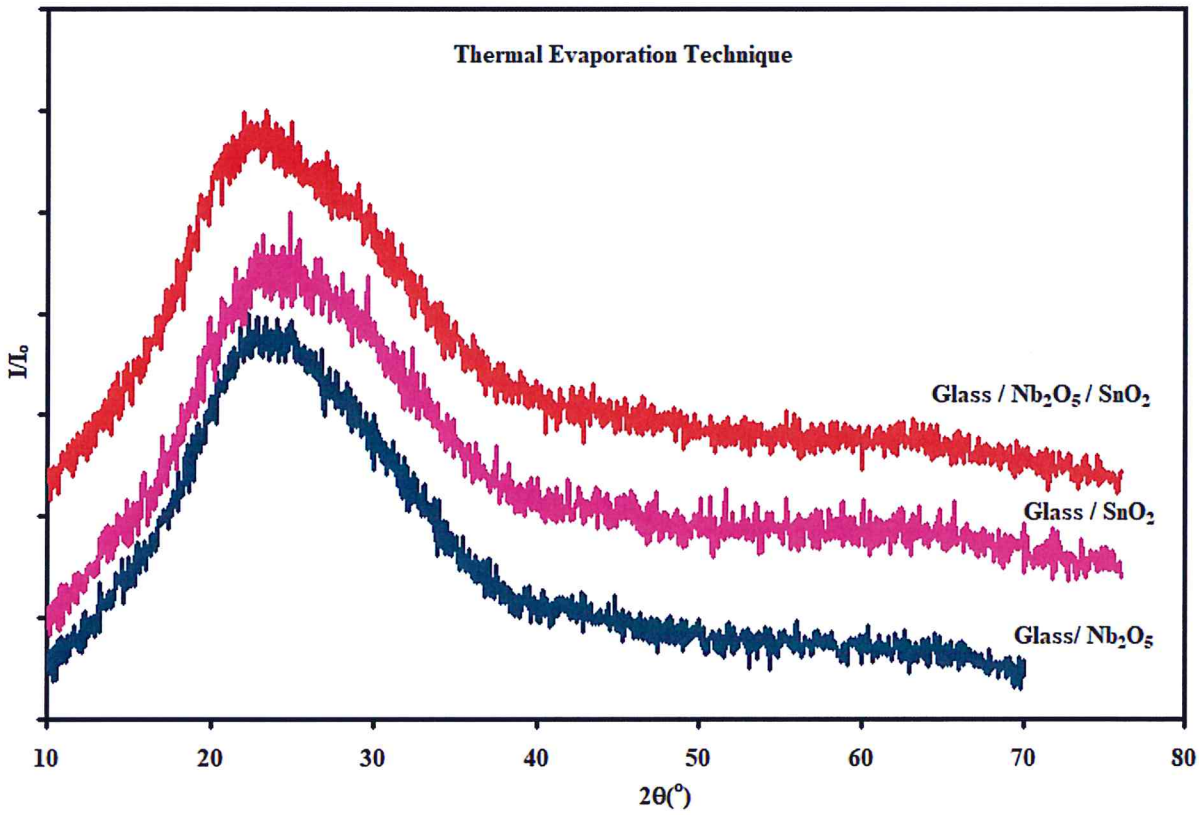

Fig 4.4. The XRD patterns of the thin films Glass/Nb_2O_5, Glass/SnO_2 and Glass/Nb_2O_5/SnO_2.

4.2 Impedance spectroscopy analysis

To investigate the electrical properties of samples prepared by the three different methods, the samples were studied by the impedance spectroscopy technique in the frequency domain of 0.01-1.80 GHz. The signal amplitude was 0.1 V. No dc biasing was employed. The measured capacitance (C), resistance (R) and inductance (L) were used to determine the impedance spectra using equation (2.19) described in theoretical approach part.

The capacitance spectra for the samples prepared by the laser welding, solid state reaction and thin films deposition techniques are illustrated in Fig 4.5(a). The respective geometrical design of the samples is shown in the insets of Fig 4.5(b), Fig 4.5(c) and Fig 4.5(d). Circular silver point contact with area of 3.14×10^{-2} cm^2 was painted on top of the samples. The bottom of the samples was fully painted with silver paste.

The capacitance spectra of the samples prepared by LW technique displayed decreasing trend of variation with increasing AC signal in the domain of 0.01-0.25 GHz. Followed by a slower trends of variation until reaching a small peaky behavior in the microwave region in which the signal display antiresonance followed by resonance phenomena near 1.53 and 1.55 GHz , respectively. Generally, resonance – antiresonance phenomena are associated with defects and surface defects and or traps. Resonance – antiresonance phenomena are usable as electronic clocks and fast switch [60]. This phenomenon is also common in quartz crystals and piezoelectric materials and usually used as Quartz Crystal Microbalance (QCM) sensor [61], foot step power generator [62], alarm clocks, and microsurgery which are monitored by magnetic resonance imaging (MRI) [63]. Moreover, resonance – antiresonance phenomena are used in wave traps [64].

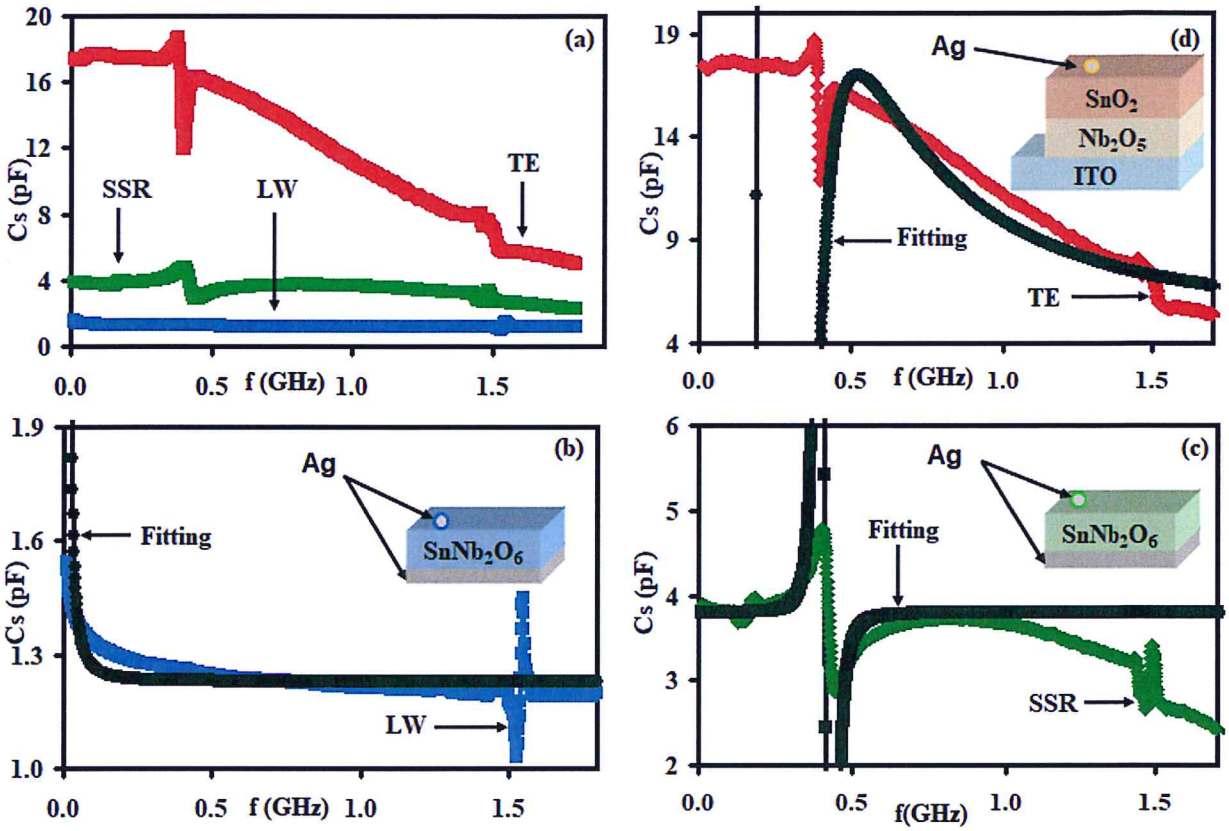

Fig 4.5. (a) The capacitance spectra for $SnNb_2O_6$ prepared by LW and SSR and $ITO/Nb_2O_5/SnO_2$ thin films prepared by TE. (b) The theoretical fitting for the capacitance spectra of samples prepared by LW (c) by SSR and (d) by TE techniques. Inset -1 of (b) shows the geometrical design of the samples prepared by LW (c) by SSR and by (d) TE techniques.

The frequency interval between antiresonance (low positive value) and resonance (high positive value) is 20 MHz which means the time required to charge and discharge the capacitance is 50 ns. This property indicates the possibility of using the devices as capacitive switches. Peaks of the same amplitude are also observed at the same position for both samples prepared by SSR and TE techniques, in which the signals display antiresonance followed by resonance at frequency of 1.469 and 1.486 GHz. The frequency interval is 17 MHz means that the system will switch within 59 ns for two techniques. On the other hand, a well pronounced peak is observed in the radio wave region of the

capacitance spectra of samples prepared by SSR and TE techniques. The capacitance spectra of samples prepared by LW didn't show such peak in that range. The signal shows resonance followed by antiresonance at frequencies of 0.406, 0.455 GHz and 0.379, 0.403 GHz. Moreover, the switching time is 20.4 ns and 41.6 ns, for samples prepared by SSR and TE techniques, respectively. The features of the samples indicate its usability as frequency based fast switches.

The frequency invariant capacitance spectra, for samples prepared by LW and SSR, are assigned to the electric dipoles being not sensing the frequency of an AC signal. This occurs when the frequency of the alternating electric field is much lesser or larger than the frequency of the electric dipoles of the material so that the capacitance does not change and is considered capacitance independent of the frequency. On the other hand, the phenomenon of resonance can be explained as follows, when the frequency of the AC signal is close to that of the electric dipoles, the dipoles respond to the AC signal and the capacitance starts to increase until it reaches a very high value and no free charge can be observed. At this point, the dipole frequency of the material (ω_{pe1} and ω_{pe2}) (material plasmon frequency) is equal to the frequency of the AC signal. When the frequency of the AC signal exceeds the electric dipole frequency of the material, the dipoles can't feel the electric field due to the short time of the oscillating field so that the capacitance begins to decrease until return to its steady state case [35,36]. The capacitance values for the thin film in the range between 5.01 - 18.71 pF, which means that the $ITO/Nb_2O_5/SnO_2$ thin films prepared by TE technique has a wide range of tunability when compared to other samples prepared by LW and SSR methods. The capacitance of thin film displays a value of 17.475 pF at 0.242 GHz and falls down to 5.203 pF at 1.75 GHz. In addition, the thin film technique has the highest values of capacitance, in

which the capacitance value ranges from 10 times and 3 times higher than capacitance of samples prepared by other techniques in radio wave and microwave ranges, respectively.

In order to theoretically analyze the behavior and discontinuity of capacitance spectra the modified Ershov and Qasrawi model in the AC conduction was taken into consideration and the amplitude spectra were reproduced using the right-hand side of equation (2.5).

The resulting parameters are shown in Table 4.8. According to the modified model, the capacitance spectra consist of two parts, the first is the geometric capacitance (C_o) which does not depend on the signal frequency. The second part is the dynamic capacitance (C_1) or relaxation part which depends on the dielectric response to the frequency of the AC signal. The dynamic capacitance is attributed to the effect of impact ionization, trapping and electron transport. The model assumes that the electrons give a positive capacitance causing resonance, and the holes give negative capacitance which causes antiresonance. By substituting the pre-exponential value $a_1 = 0.15$ F/s , the relaxation time constant $\tau =$ 10 μs and the electron plasmon frequency $\omega_1 = 0.01\,GHz$ in the equation (2.5), the theoretical capacitance spectrum of the sample prepared by LW method presenting by the black curve shown in Fig 4.5(b) was produced. Furthermore it, the theoretical amplitude spectra for the samples prepared by SSR and by TE techniques shown in Fig 4.5(c) and Fig 4.5(d) are obtained assuming the values shown in Table 4.8. The tabulated data indicate that the geometrical capacitance values varies with the preparation technique. The stacked layer thin films show the largest value of 5 pF. C_o values for samples prepared by SSR and LW method are 3.80 and 1.23 pF, respectively.

From the geometrical capacitance, the microwave cut off frequency f_{CO} ($f_{co} = \frac{G}{2\pi C} = \frac{1}{2\pi RC}$) , where R is the resistance,C is the geometrical capacitance [65] can be determined. It

indicate the value of the lowest signal frequency which is allowed to propagate through the sample. Hence, the studied samples can be used as a waveguide and signals propagate above the value of f_{co} . On the other hand, the dynamic capacitance with the value $a_2 = 0$ for the sample prepared by laser method indicates that there is only one type of charge carriers in bulky samples. The capacitance which arises from holes begins to participate in the samples prepared by SSR and TE techniques. It is noticable that samples prepared by SSR technique has the highest value of the plasmon frequency of 2.5 GHz, which can be attributed to the highest free carrier density. So for signal propagation, SSR technique is preferable as it has the highest plasmon frequency.

Table 4.8: the capacitance fitting parameters for LW, SSR and TE techniques.

Parameter / Technique	LW	SSR	TE
C_o (pF)	1.23	3.80	5.00
τ_1(μs)	10	90	100
τ_2(μs)	0	80	4
a_1 (F/s)	0.15	0.10	2.50
a_2 (F/s)	0	0.10	162
ω_1 (GHz)	0.01	2.50	0.20
ω_2 (GHz)	0	2.70	1.60
f_{co} (GHz)	0.08	0.07	0.58

From the measured conductance spectra, the resulting conductivity spectra are calculated according to the equation (2.7) mentioned in theoretical part. As it is readable from the Fig 4.6 which represent the variation of conductivity with frequency, the conductivity of the samples prepared by LW technique increased timidly with increasing the signal frequency, then a small peak appeared at 1.513 GHz, followed by a decrease in the conductivity values

showing negative conductivity values at 1.549 GHz. Large similarity between the conductivity spectra of the samples prepared by LW and by SSR method can be observed, It displays two peaks, one of which is almost at the same position as that of the laser peak, with a higher conductivity value. The second sharp peak appears in the radio wave region at 0.416 GHz. the pure negative conductivity appears at a frequency greater than 1.539 GHz.

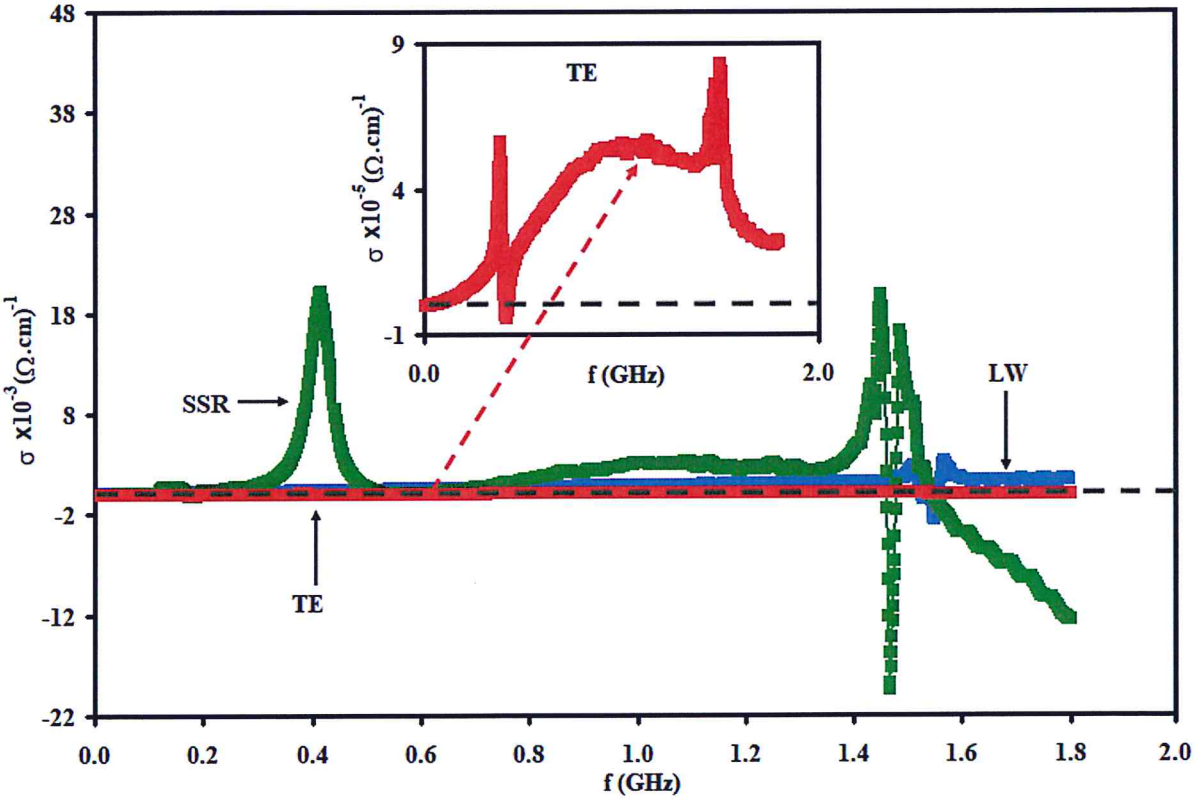

Fig 4.6. The conductivity spectra for the samples prepared by LW, SSR and TE techniques. Inset - 1 is an enlargement of the conductivity spectra of the ITO/Nb_2O_5/SnO_2thin films prepared by TE technique.

The negative differential conductance effect (NDC) was previously observed in the two stacked layers of Se thin film sandwiched between Au and In metals, NDC effect was attributed to the formation of thin potential barriers at the Au/Se and In/Se interfaces where

free charge carriers are tunneling through these barriers [66]. NDC also appears in Cu_2O/Au thin film after deposition of monolayer copper islands onto the films [67]. NDC is important property for applications of Nano-electronic devices such as switches, smart control system, gas sensing and amplifiers [68]. The effect of NDC correlates with resonance of capacitance, so it is attributed to the defect and trap effect that leads to coulomb repulsion and tunneling at the interface with the Ag contact (quantum interface). As shown in Fig 4.6. The conductivity of the $ITO/Nb_2O_5/SnO_2$ thin films prepared by TE is two orders of magnitude lower than that of ceramics prepared by SSR and $SnNb_2O_6$ bulk prepared by LW techniques due to the growth nature of the samples (2D material). The conductivity behavior of the thin film is enlarged in inset -1 of Fig 4.6. As can be seen from the figure, the conductivity increased sharply with increasing frequency reaching a maximum value at 0.388 GHz. It, then, decreases sharply reaching a negative value at 0.415 GHz. The conductivity spectrum shows resonance and anti-resonance phenomena from positive to negative value. The conductivity increases sharply in the region 0.415 - 0.900 GHz, then reaches the saturation level in the region 0.900 - 1.430 GHz. As the frequency exceeds 1.506 GHz, the conductivity reaches an absolute maximum peak, followed by a decreasing trend of variation. It is interesting to mention that for the three techniques, the frequency values where the capacitance displays resonance - anti resonance matches with the frequency values where the maximum conductivity is observed.

These AC conductivity behaviors can be attributed to the presence of more than one conduction mechanisms in the samples. Namely, quantum mechanical tunneling (QMT) and barrier hopping conduction mechanism (CBH) [69]. Mostly QMT predominates in regions where conduction increases with increasing signal frequency. On the other hand, CBH

which is a phonon assisted conduction mechanism dominates in the region where the conductivity decreases with increasing signal frequency.

To analyze the behavior of electrical conductivity as a function of signal frequency, the current conduction mechanisms CBH and QMT, are employed to the model of the conductivity spectra. The experimental conductivity data were reproduced by employing the equations of QMT equation (2.11) and CBH equation (2.13) from theoretical part. The equations which reproduce the experimental data were treated by designing a template to reproduce experimental data. The theoretical conductivity spectra for samples produced by the three techniques and the fitting Parameters used to reproduce the conductivity spectra are illustrated in Fig 4.7 and Table 4.9, respectively. As it clear from the Fig 4.7(a), the experimental measurement was successfully reproduced for samples prepared by laser method in the frequency domain of 0.01-1.45 GHz. The CBH method predominates in samples produced by the laser method only. The fitting of the CBH equation is shown by solid line in Fig 4.7(a). No evidence of the QMT method was observed.

For samples prepared by SSR technique, QMT is dominant in the frequency range of 0.303 - 0.415 GHz. This result is shown by the pink solid line in the Fig 4.7(b). The conductivity increased sharply with increasing frequency. In the frequency range 0.417 - 0.527 GHz where the conductivity decreased sharply with increasing signal frequency, it was not reproducible as it required deeper analysis and could be considered as a transition period between the QMT and CBH conduction mechanisms.

The conductivity data for samples prepared by TE technique were reproduced by executing the fitting, assuming two distinct solutions below and above 0.427 GHz as represented in Fig 4.7(c) and Fig 4.7(d), respectively. The QMT process is dominant in the frequency

domain of 0.153 - 0.388 GHz. For larger applied frequencies, CBH is dominant. By neglecting the sharp peak observed at 0.388 GHz, the second solution was reached. As seen from Fig 4.7(d), the solution indicated the domination of the two current mechanism in the samples.

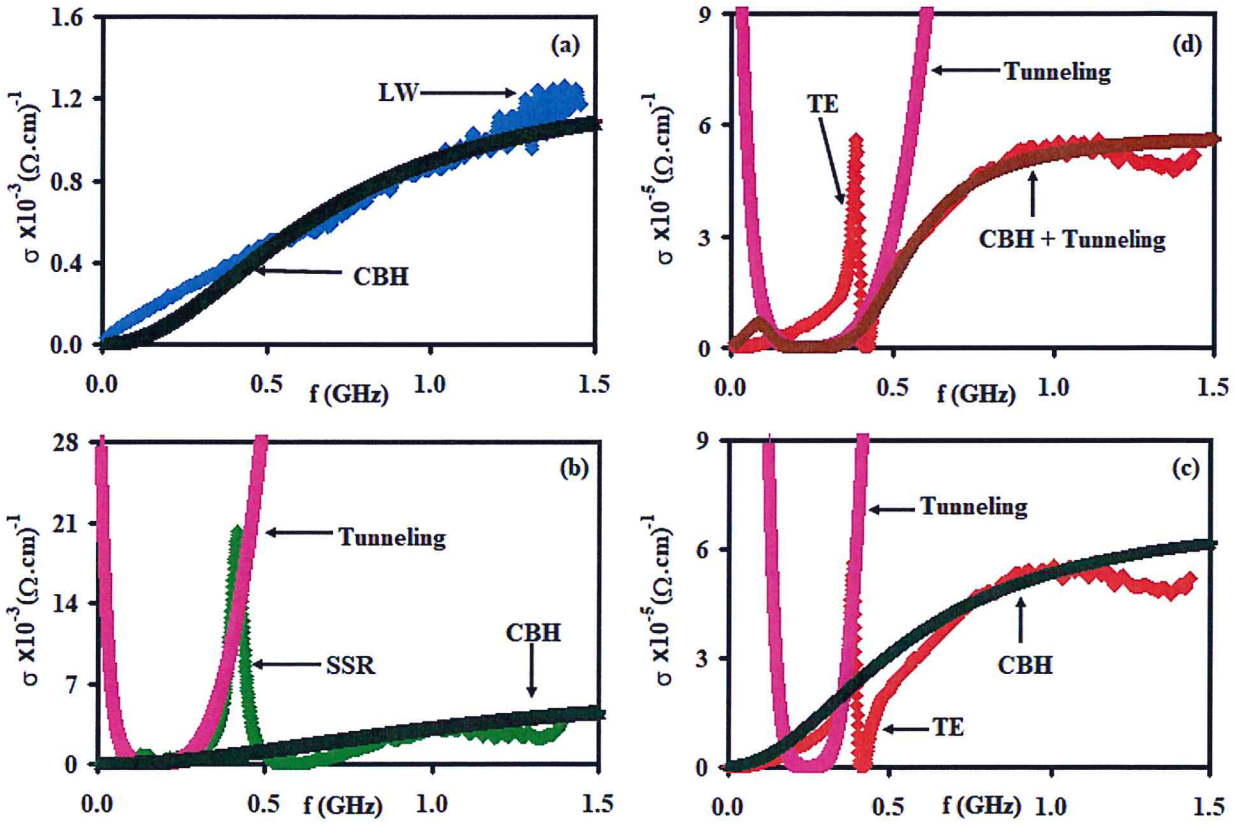

Fig 4.7. (a) the theoretical fitting of the conductivity for the samples prepared by LW technique and (b) by SSR technique (c) the first solution for samples prepared by TE technique for f < 0.427 GHz (d) the second solution for samples prepared by TE technique for f > 0.427 GHz.

As it clear from the numerical values shown in the Table 4.9, the density of localized state around the Fermi level $N(E_f)$ of the samples prepared by SSR technique is very high compared to samples prepared by TE technique. The reason for this large value of SSR

sample may be due to the concentration of high defects. Comparing the conductivity values at low frequencies, it is seen that the samples prepared by TE technique are more conductive compared to that of the samples prepared by LW and SSR techniques. On the other hand, samples prepared by SSR technique have very high conductivity values compared to samples prepared by LW and TE techniques. It means that SSR technique is more appropriate at high frequency. As the Table also shows, the scattering time at nanosecond level is larger for samples prepared by SSR method. The hopping time constant is shorter in samples prepared by SSR method compared to samples prepared by TE and LW methods.

Table 4.9 : The AC conductivity parameters for LW, SSR and TE techniques.

Technique / Parameter	LW	SSR	TE	
			$f < 0.425$GHz	$f > 0.425$ GHz
τ_0 (ns)	-	6.00	4.00	4.20
τ_{hop} (ns)	1.50	0.90	8.33	5.00
$N(E_F)$ ($x10^{20}$ $cm^{-3}eV$)	-	37	10.00	2.50
$\sigma(L)$ x (10^{-6} $\Omega^{-1}cm^{-1}$)	0.03	0.10	0.50	1.00
$\sigma(H)$ x ($10^{-3}\Omega^{-1}cm^{-1}$)	1.30	7.00	0.07	0.06

The impedance spectra (Z) of samples prepared by various techniques are computed from the measured capacitance, resistance and inductance spectra. For this purpose equation (2.19) were employed. As shown in the Fig 4.8, the impedance decreases sharply with increasing the signal frequency in the range of 0.01-0.50 GHz, with a large value of impedance in the radio wave region, then slowly decreasing with increasing the signal frequency and exhibiting a low resistance value in the microwave wave region. It is clear from the figure that 3 - spectra display a minor peak near ~1.57 GHz regardless of the

sample preparation technique. Another peak appeared in the radiowave frequency domain near ~ 0.45 GHz. This peak is absent from Z- spectra of samples prepared by LW technique. It is also evident that the samples prepared by LW exhibit highest impedance values.

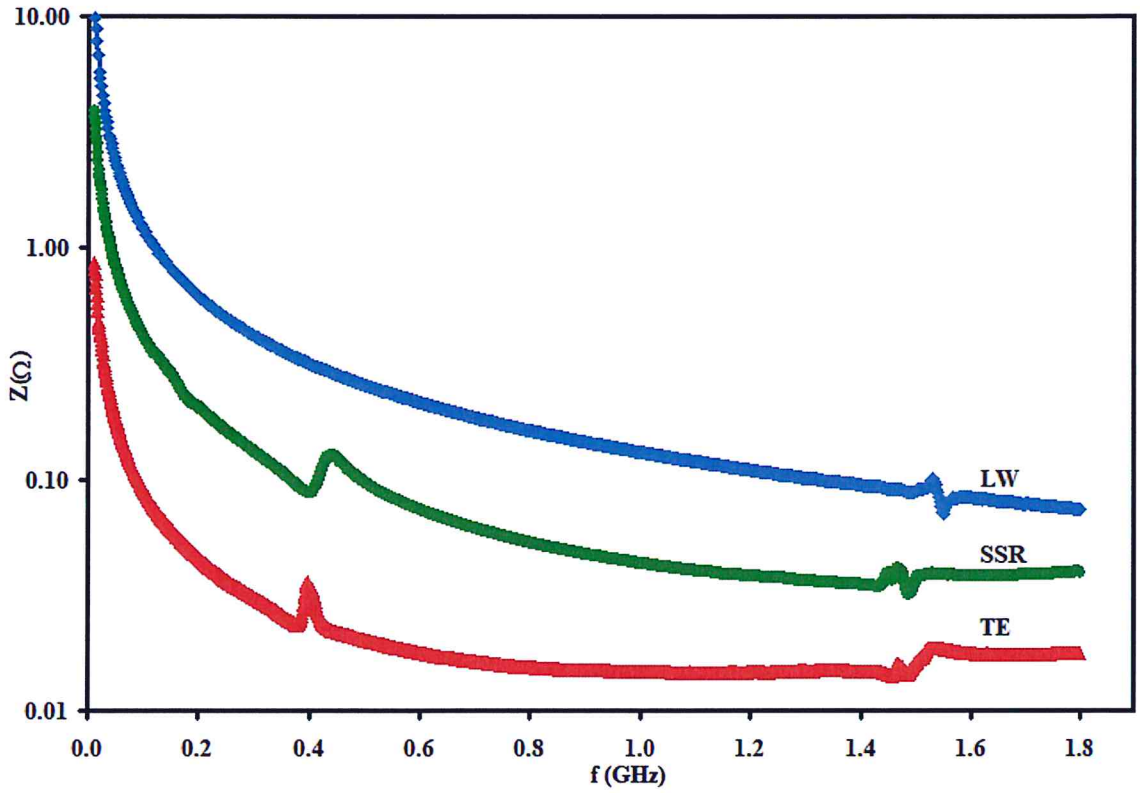

Fig 4.8. The impedance spectra for the samples prepared by LW, SSR and TE techniques in the spectral range of 0.01-1.80 GHz.

4.3: Current -Voltage Characteristics

The Ohmic nature of the silver contacts of the samples prepared by laser welding, SSR and thin film techniques are verified by the current (I)- voltage (V) characteristic curves which are shown in Fig 4.11(a), (b) and (c), respectively. The I-V plots exhibit a linear relationship recorded in the voltage range of -10-10 V, - 1-1 V and -0.25-0.25 V in 0.5 voltage steps for

samples prepared by LW, SSR and TE, respectively. The respective slopes of the linear plots of the I-V characteristics at 300 K, where the slopes represent the reciprocal of the resistance, allow determining electrical conductivities of values of $1.0 \times 10^{-5}, 1.28 \times 10^{-6}$ and 1.71×10^{-4} $(\Omega.\,\mathrm{cm})^{-1}$. As can be seen from the electrical conductivity values of the three techniques, the electrical conductivity of the samples prepared by LW technique is one order of magnitude less than that of the samples prepared by TE technique. On the other hand, the samples prepared by SSR technique gives two order of magnitude less conductivity compared to the sample prepared by TE technique.

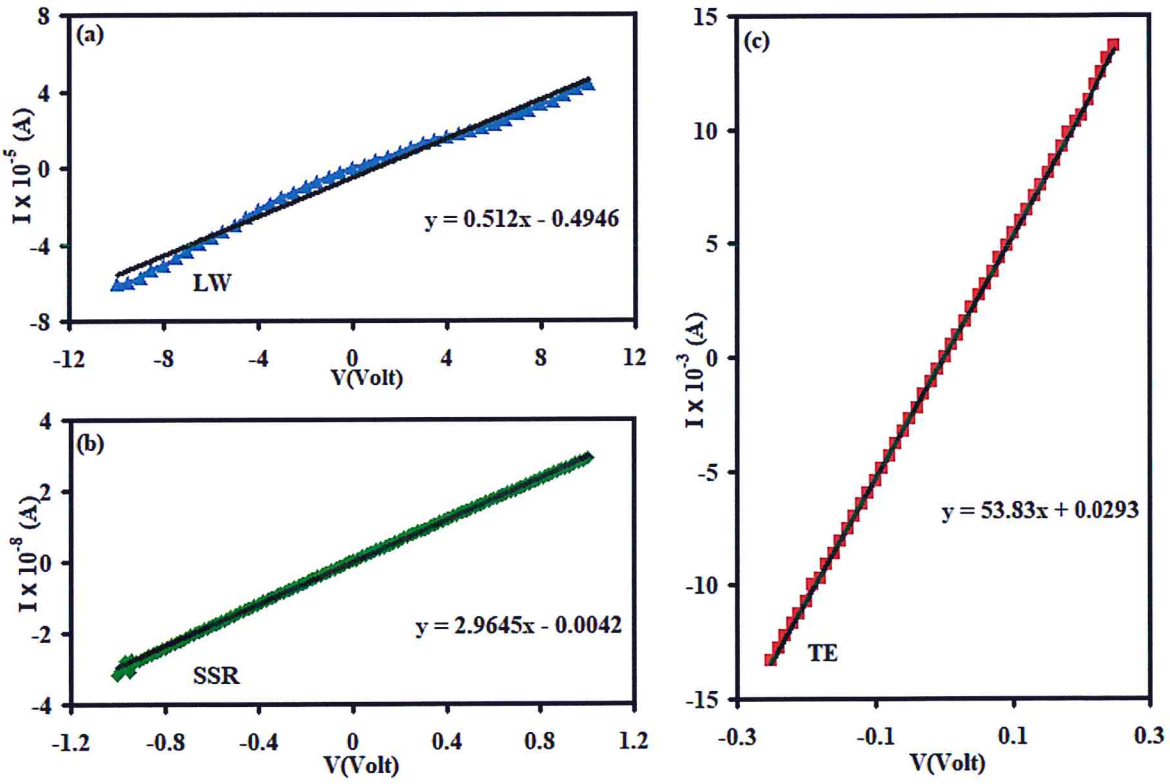

Fig 4.9. (a) The Current-Voltage characteristics at room temperature for the samples prepared by LW technique (b) by SSR technique and (c) by TE techniques.

4.4: Optical analysis

From samples prepared by the thin film stacking layers technique, which is used to prepare Nb_2O_5, SnO_2 and Nb_2O_5/SnO_2 thin films on glass substrates, the optical properties of three samples are studied via ultra- violet visible light spectrophotometry technique. To obtain these properties, the optical transmittance (T) and optical reflectance (R) spectra were analyzed.

The optical transmittance spectra as a function of the incident light wavelength in the range of 300-1100 nm for the three samples are shown in Fig 4.10(a). For $Glass/Nb_2O_5$, the transmittance of incident light increased sharply with increasing wavelength and reaches a maximum at 378 nm (3.29 eV). For larger λ value, saturation in transmittance spectra predominates. The transmittance has high values when the energy of incident light is less than or equal to the energy band gap of the material.

The transmittance of incident light increases sharply with increasing wavelength until reaching a wavelength of 430 nm (2.89 eV) and to 412 nm (3.02 eV) in $Glass/SnO_2$ and $Glass/Nb_2O_5/SnO_2$ thin films, respectively. Then the transmittance increases slightly with increasing the wavelength of both film. As can be seen from Fig 4.10(a), the transmittance of $Glass/Nb_2O_5$ is the highest. Whereas, the addition of the SnO_2 layer over Nb_2O_5 layer reduced the transmittance of $Glass/Nb_2O_5$. The transmittance of thin films does not reach zero due to high transparency of the films.

As can be seen from Fig 4.10(b) which represents the variation of the reflection coefficient spectra, the reflection of the incident light of $Glass/SnO_2$ is the highest. The reflection coefficient spectra for $Glass/SnO_2$ and $Glass/Nb_2O_5/SnO_2$ thin films show one interference pattern in the wavelength range of 400 - 600 nm. R spectra of $Glass/SnO_2$

films display a peak at 448 nm (2.77 eV). It redshifts to 490 nm (2.54 eV) for Glass/Nb_2O_5/SnO_2 stacked layer.

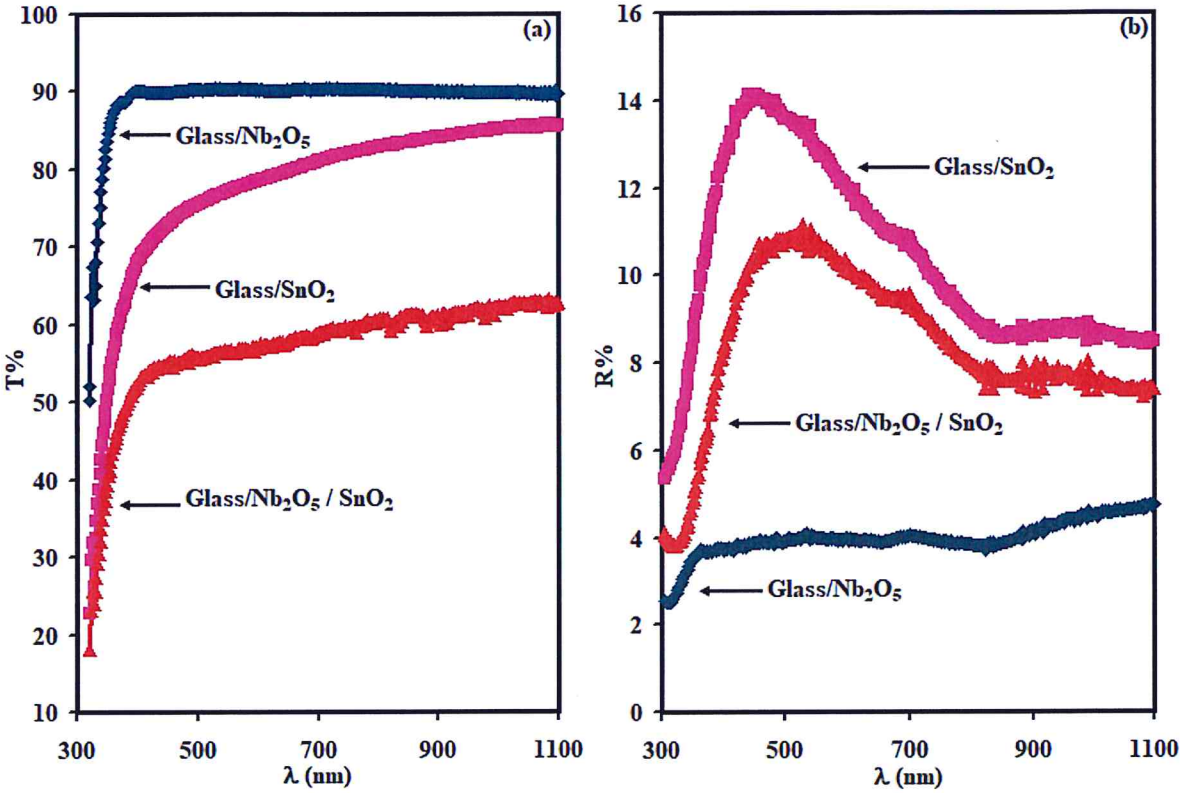

Fig 4.10. (a) The transmittance, (b) the reflectance for Glass/Nb_2O_5, Glass/SnO_2 and Glass/Nb_2O_5/SnO_2thin films.

The transmittance and reflectance measurements are employed to find the absorption coefficient (α) spectra through equation (2.22) for the Glass/Nb_2O_5 and Glass/$SnO_2$and Glass/Nb_2O_5/SnO_2 thin films. The variations of the absorption coefficient with the incident photon energy for Glass/Nb_2O_5, Glass/SnO_2 and Glass/Nb_2O_5/SnO_2 thin films are presented in Fig 4.11(a). The lowest values of α are observed for Glass/Nb_2O_5 thin film. Two distinct absorption regions appeared in α- spectra of the studied samples. Namely, the strong absorption region in the range of 3.0- 3.9 eV and the low absorption region in the

range of 1.1-3.0 eV. In addition, a non-zero value of the absorption coefficient is observed indicating the presence of interbands or band tails [45]. For Glass/Nb_2O_5 thin films, the absorption is sharp in the region above 3.5 eV. Below this value the absorption coefficient is invariant indicating formation of the interbands in the film. The interband arises from defects and broken bonds [45]. The thin films of Glass/SnO_2 and Glass/Nb_2O_5/SnO_2 show high absorbability in the region above 3.0 eV. Below 3.0 eV the absorption coefficient decreases smoothly indicating the presence of band tails. This range is shown in the inset of Fig 4.11(a). Band tails are usually resulting from charge impurities, broken bonds and defects.

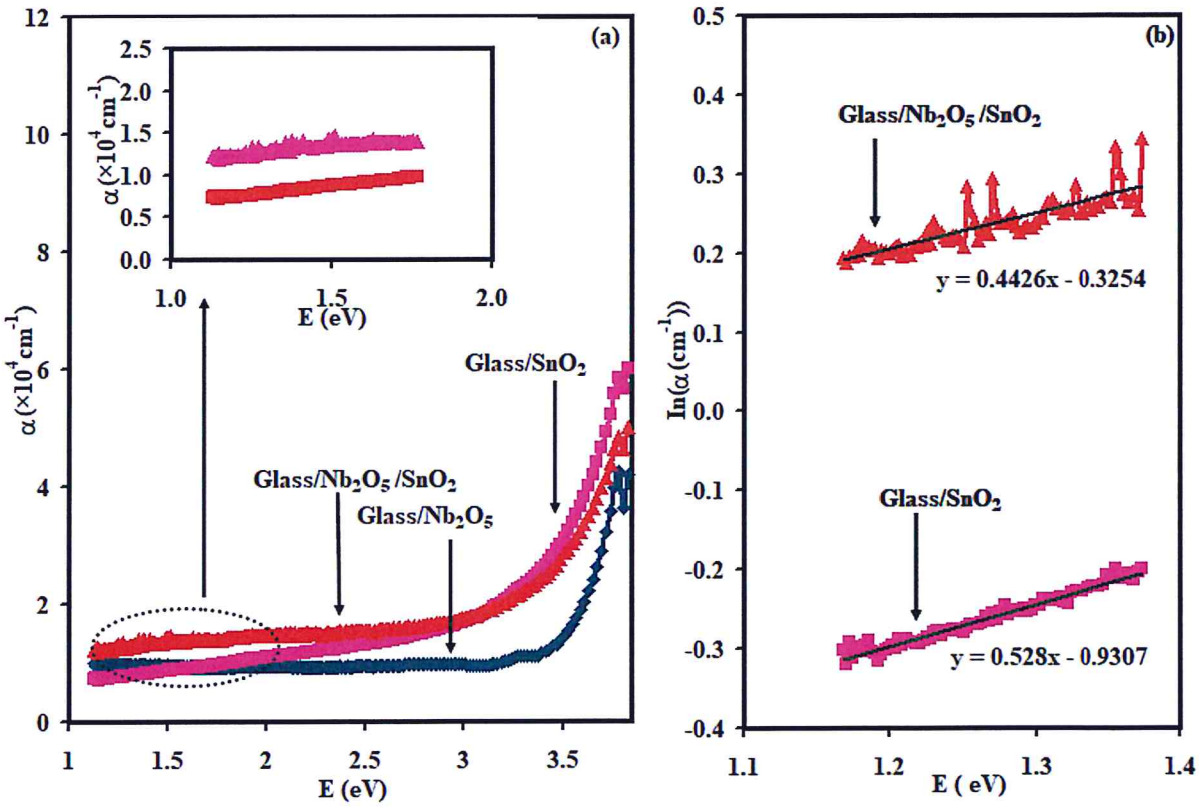

Fig 4.11. (a) The absorption coefficient spectra for Glass/Nb_2O_5, Glass/SnO_2 and Glass/Nb_2O_5/SnO_2 thin films, (b) the $Ln(\alpha) - E$ variations for Glass/SnO_2 and Glass/Nb_2O_5/SnO_2 thin films. Inset 1 of (a) shows the absorption coefficient spectra of Glass/SnO_2 and Glass/Nb_2O_5/SnO_2 thin films in the visible light region.

To determine the width of the band tails at low incident photon energy, the Urbach rule's equation (2.24) is employed. From the reciprocal of the linear slope of the linear relations of the Ln(α) – E variations shown in Fig 4.11(b) the band tail widths (E_e) are determined, values of E_e= 1.89 and 2.26 eV are estimated for the films Glass/SnO_2 and Glass/Nb_2O_5/SnO_2 thin films, respectively. Stacking of SnO_2 over Glass/Nb_2O_5 widens the band tails. However, as E_e exist in the energy band gap they should be less than half of the energy band gap ($E_e < \frac{E_g}{2}$), which is not observed for our studied samples. Hence, the decreasing trend of variation of $\alpha - E$ variations in the low absorption region can be assigned to the existence of more than one energy band gap in Glass/SnO_2 and Glass/Nb_2O_5/SnO_2 thin films.

The optical energy band gap is determined from the absorption coefficient spectra by applying the Tauc's equation (2.23). The best linear relation was verified for $(\alpha E)^2$ as a function of the incident photon energy, as shown in Fig 4.12. thus, direct allowed transition is dominant in the three films, and the direct allowed energy band gap values evaluated from the E-axis crossing are 3.62, 3.53, and 3.53 eV for Glass/Nb_2O_5, Glass/SnO_2, and Glass/Nb_2O_5/SnO_2, respectively.

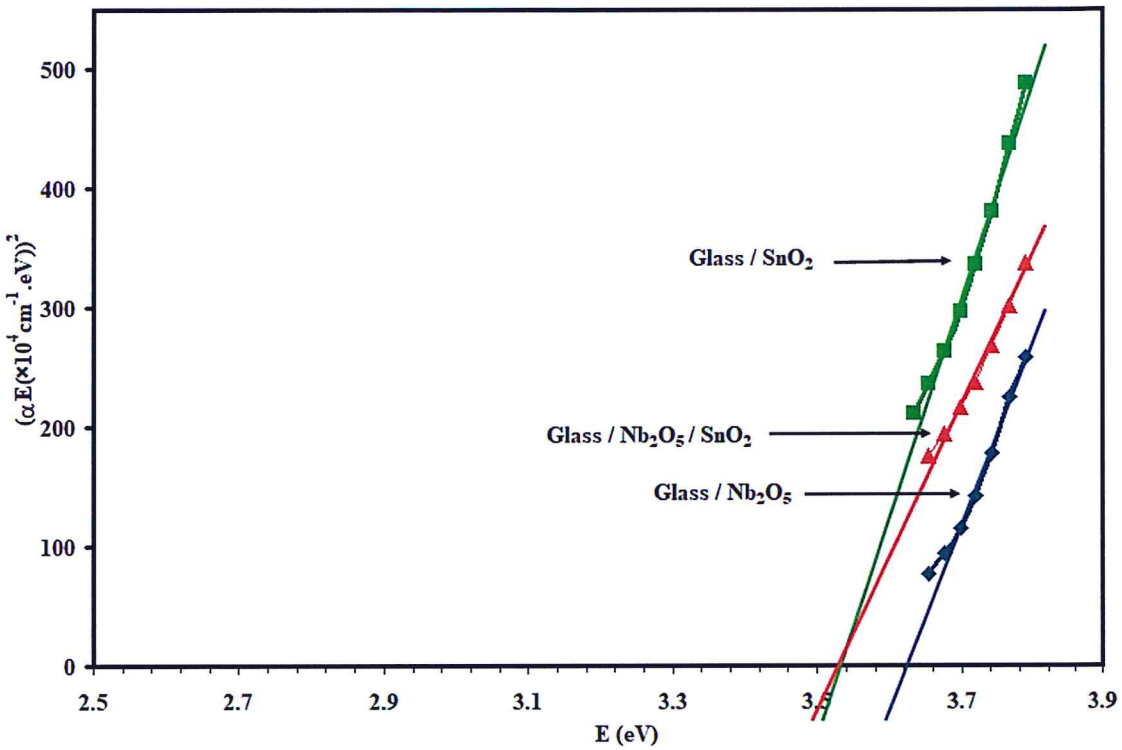

Fig 4.12. The Tauc's equation fittings for Glass/Nb_2O_5, Glass/SnO_2 and Glass/Nb_2O_5/SnO_2thin films.

The energy band gap value of Nb_2O_5 is consistent with the literature data [70]. In addition, thin films of Nb_2O_5 which were deposited onto a metal substrate and doped with 0.1 Nb Prepared using a hydrothermal method displayed a direct allowed transitions energy band gap of 3.3 eV [71]. An energy gap of 3.52 eV is reported for SnO_2 thin film was already reported in the literature data [72]. Moreover, the spray pyrolysis prepared SnO_2 nanostructured thin films doped with Mg (1%) showed similar energy gap value and the same transition [73]. It is also worth mentioning that the energy band gap values were in the range of 2.35 - 3.43 eV are obtained when $(SnO_2)_x(ZnO)_{1-x}$ thin films with different concentrations of SnO_2 and ZnO were deposited by using electron beam evaporation technique [74]. On the other hand, stacked layer Nb_2O_5/SnO_2 thin films showed a different

energy gap value compared to the heterostructure Nb_2O_5/SnO_2 prepared by hydrothermal method [24].

The dielectric properties of $Glass/Nb_2O_5$, $Glass/SnO_2$, and $Glass/Nb_2O_5/SnO_2$ were investigated for the materials, to determine the optical conduction properties and to identify possible applications of the double layer thin film. From the measurements of transmittance and reflectance with the help of the Fresnel's equation for normal incident light, the real and imaginary part of the dielectric spectra are calculated according to the previously mentioned equation (2.35) and equation (2.36). For data demonstration using equation (2.41) a simulation template were designed to produce effective dielectric spectra.

As shown in Fig 4.13 which represents the variation of the real part ε_r of the dielectric constant with the energy of the incident light, evaporation of SnO_2 layers onto $Glass/Nb_2O_5$ layers improved the dielectric property of $Glass/Nb_2O_5$.The ε_r for $Glass/Nb_2O_5/SnO_2$ double layer exhibit similar trend of variation to that of $Glass/SnO_2$ but with lower values. Also, the nonlinear behavior of the dielectric constant with photon energy indicates the suitability of these thin films for nonlinear optical applications. As Fig 4.13 shows, for amorphous $Glass/Nb_2O_5$ thin films, ε_r spectrum exhibit broaden peak in the dielectric constant at 1.78 eV with maximum dielectric constant value of 2.25. This change can be assigned to the interband transition that arises from defects and broken bonds. The dielectric constant of $Glass/Nb_2O_5$ also shows another broaden peak at energy value of 3.41 eV with ε_r value of 2.19. This broaden peak may be attributed to the indirect allowed optical transitions since this value is close to the energy gap value of the sample.

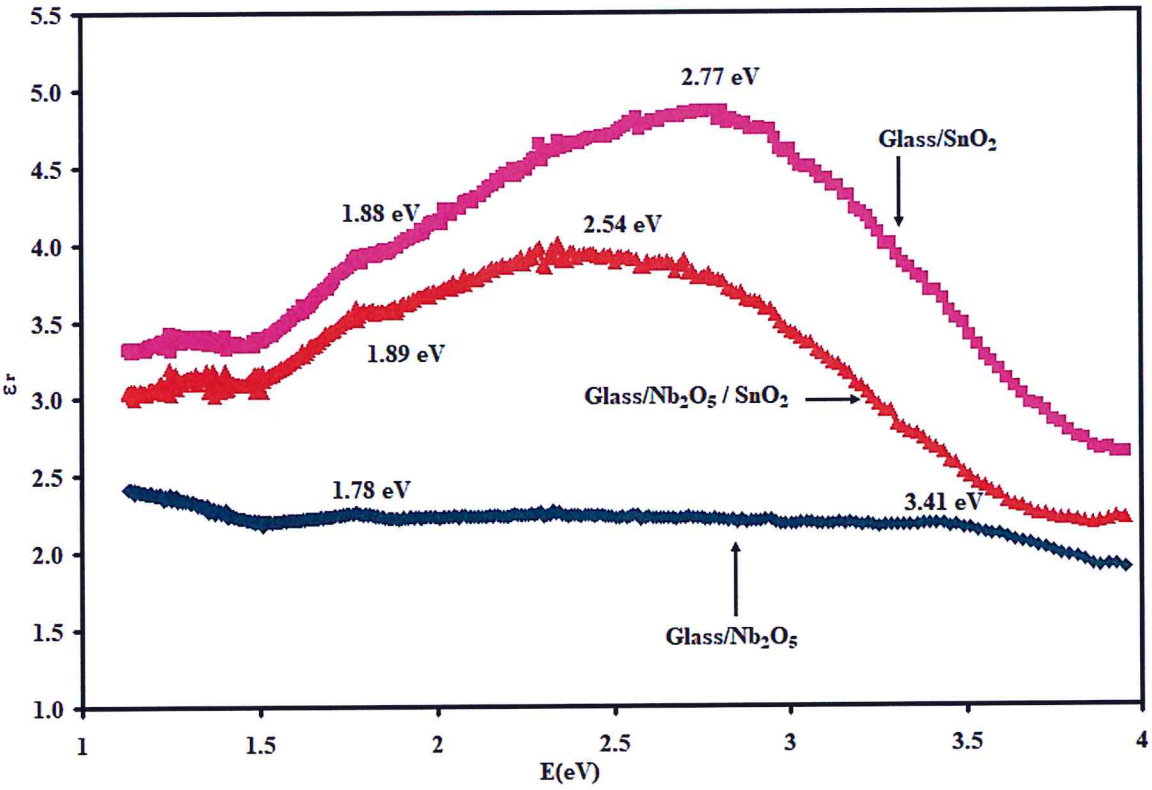

Fig 4.13. The real part of the dielectric spectra for Glass/Nb_2O_5 Glass/SnO_2 and Glass/Nb_2O_5/SnO_2.

The dielectric spectra of SnO_2 has a broaden resonating peak centered at 2.77 eV. This peak shifts to 2.54 eV in the Glass/Nb_2O_5/SnO_2thin film. The maximum values of ε_r being 4.86 and 3.92 for SnO_2 and Glass/Nb_2O_5/SnO_2thin films, respectively. Shoulders are observed at 1.88 eV, with ε_r values of 4.00 and 3.5 for the Glass/SnO_2 and Glass/Nb_2O_5/SnO_2 thin films, respectively. The presence of the wide resonant peak centered at 2.77 and at 2.54 eV for Glass/SnO_2 and Glass/Nb_2O_5/SnO_2 thin films, respectively, are attributed to the indirect allowed transitions. On the other hand, the changes in the dielectric spectra at 1.88 eV and 1.89 eV are due to electron – electron interactions [75].

The optical conductivity parameters, hole motion and plasmon - hole interaction can be detected by analyzing the imaginary part of the dielectric constant. The imaginary part of the dielectric constant as a function of the incident photon energy of Glass/Nb_2O_5, Glass/SnO_2 and Glass/Nb_2O_5/SnO_2 are illustrated of Fig 4.14. It is evident from Fig 4.13 and Fig 4.14 that the values of ε_{im} are less than those of ε_r by one order of magnitude at least.

It is also noticeable that, the value of ε_{im} decreased with increasing the energy of the incident photon up to 3.5 eV and then increased sharply in the range of 3.5 - 3.9 eV for both Glass/Nb_2O_5 and double layers thin films but with lowest values of ε_{im} for the Glass/Nb_2O_5 thin film. The imaginary part of the dielectric constant of SnO_2 increases slightly with increasing photon energy in the range of 1.1-3.5 eV. As the energy exceeds 3.5 eV, ε_{im} increases sharply with increasing photon energy. It is evident that the coating of SnO_2 layers over Glass/Nb_2O_5 films increased the ε_{im} value of Glass/Nb_2O_5, implying an improvement in optical conduction.

In order to reveal information about optical conductivity parameters ($\sigma(\omega) = (\varepsilon_{im}\omega/4\pi)$), hole motion, and plasmon-hole interaction in samples, the imaginary part of the dielectric constant spectra is modeled in accordance with Drude-Lorentz's model through the equation [76].

$$\varepsilon_{im}(\omega) = \sum_{i=1}^{k} \frac{{\omega_{pei}}^2 \omega}{\tau(({\omega^2}_{ei} - \omega^2)^2 + \omega^2 {\tau_i}^{-2})} \qquad (4.1)$$

Where k is i the number of linear oscillators and ω is the angular frequency of incident light.

The fitting which is achieved by the equation (4.1) provide information about the values of hole scattering time (τ), reduced resonant frequency (ω_e), hole bounded plasma frequency ($\omega_{pe} = \sqrt{4\pi ne^2/m^*}$), free hole density (p) and drift mobility($\mu = e\tau/m^*$) for the three samples. The conductivity type of both SnO_2 and Nb_2O_5 thin films are p - type as determined using the hot probe technique.

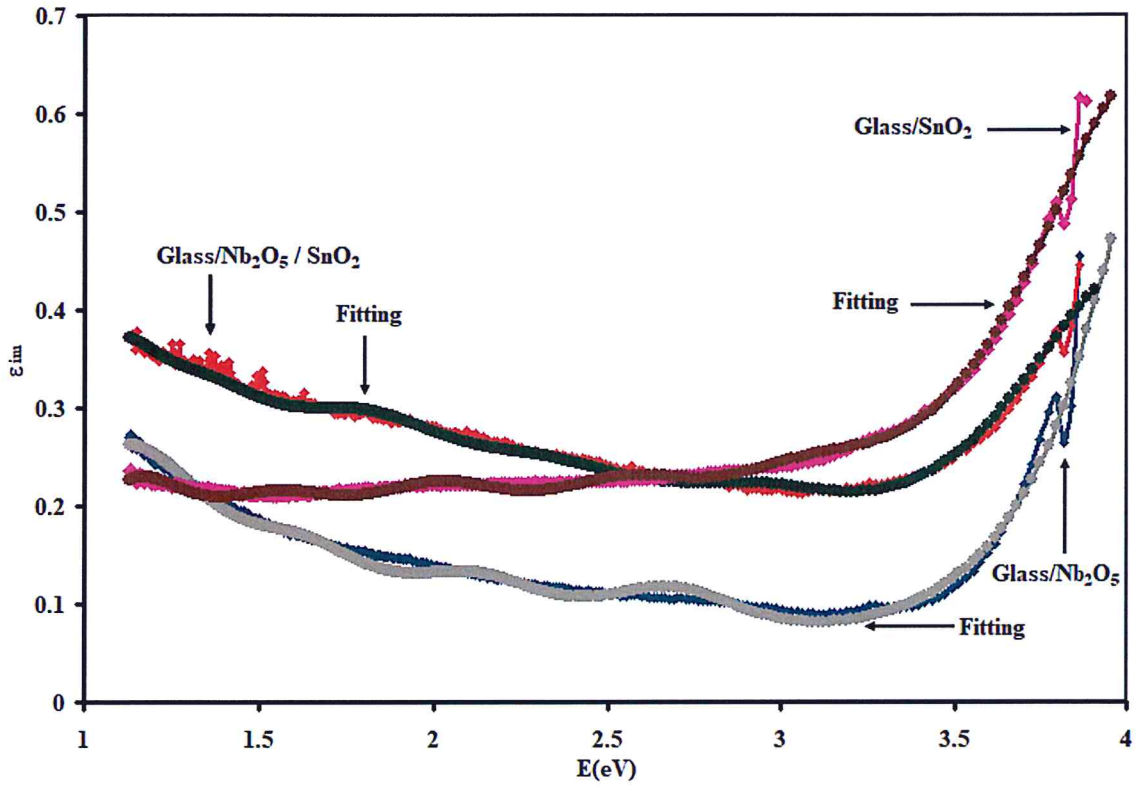

Fig 4.14. The imaginary part of the dielectric spectra for Glass/Nb_2O_5, Glass/SnO_2 and Glass/Nb_2O_5/SnO_2 thin films. The solid gray, brown and black spectra are the results of the fitting of equation (4.1).

The experimental data were reproduced by running the series of equation (4.1) up to k = 6. The hole effective mass values in Glass/Nb_2O_5 and Glass/SnO_2 are $m^*_{Nb_2O_5} = 0.959\ m_o$ [77], and $m^*_{SnO_2} = 0.25\ m_o$ [78]. The effective mass of the Nb_2O_5/SnO_2 double layers is

calculated from the equation [45] $m^*_{Nb_2O_5/SnO_2} = (\frac{1}{m^*_{Nb_2O_5}} + \frac{1}{m^*_{SnO_2}})^{-1}$ and found to be 0.198 m_o. The theoretical data marked by the gray, brown and black colored fitting curves are displayed in Fig 4.14 for Glass/Nb_2O_5, Glass/SnO_2 and Glass/Nb_2O_5/SnO_2 thin films, respectively. There is good correlation between the experimental and theoretical data as shown in figure for the three thin films.

The optical conductivity parameters that yield from the fitting process are tabulated in Table 4.10. The hole scattering time equals the inverse of the damping coefficient ($\gamma = \tau^{-1}$) decreases with increasing number of oscillators for all samples.

For all samples, the higher the oscillator frequency (ω_e) the shorter the scattering time, the larger the damping coefficient, the higher the electronic friction. Such behavior is assigned to defects. Namely, when the photon energy is high and sufficient to activate more defects and trap centers, the scattering time decreases and, thus, the number of holes aligned in the electric field direction decreases leading to a decrease in the hole mobility.

The increase in the charge carrier concentration (free holes) is accompanied by a decrease in the drift mobility values [54]. The plasma frequency also increased with the increasing oscillator frequency, indicating there were a large number of free holes.

Table 4.10: The optical conduction parameters for Glass/Nb_2O_5, Glass/SnO_2 and Glass/Nb_2O_5/SnO_2 thin films

	Glass/Nb_2O_5						Glass/SnO_2						Glass/Nb_2O_5/SnO_2					
m^*/m_o	0.959						0.250						0.198					
i =	1	2	3	4	5	6	1	2	3	4	5	6	1	2	3	4	5	6
τ_i (fs)	1.50	1.20	1.10	1.10	1.10	1.10	1.30	1.00	0.90	0.90	0.80	0.70	1.60	1.00	0.80	0.70	0.70	0.68
p_i (x 10^{17} cm^{-3})	36	45	47	49	60	800	13	15	24	26	33	340	11	16	27	28	29	183
ω_{ei} (x 10^{15} Hz)	1.62	1.90	2.50	3.25	4.10	6.25	1.75	2.40	3.11	3.90	4.70	6.19	1.65	2.10	2.80	3.60	4.50	6.14
E_e (eV)	1.06	1.25	1.64	2.13	2.69	4.10	1.15	1.58	2.04	2.56	3.08	4.06	1.08	1.38	1.84	2.36	2.95	4.03
ω_{pei} (GHz)	1.15	1.29	1.32	1.34	1.49	5.43	1.35	1.46	1.84	1.92	2.16	6.93	1.40	1.69	2.17	2.23	2.27	5.71
μ_i (cm^2 / Vs)	2.75	2.20	2.02	2.02	2.02	2.02	9.14	7.03	6.33	6.33	5.63	4.92	14.19	8.87	7.09	6.21	6.21	6.03

As is evident from the table values, the hole scattering time for the first oscillator is 1.5 fs and 1.3 fs for the Glass/Nb_2O_5 and Glass/SnO_2 thin films, respectively. It increased to 1.6 fs when the double layer is formed. Then, the scattering time of other oscillator in the double layer becomes the least compared to the scattering time of Glass/Nb_2O_5 and Glass/SnO_2.This means that the damping rate and the resistance of the double layer is the largest and this corresponds to the fact that the interfacial electronic interactions causes electron friction with a greater values associated with bilayer formation [79].

The drift mobility of the double layer show the highest values compared to the Glass/Nb_2O_5 and Glass/SnO_2 thin films which is equal to 14.19 cm^2/Vs for the first oscillation of the double layer. Assuming the first oscillation, The hole density in Glass/Nb_2O_5 and in Glass/SnO_2 are found to be 3.6 $\times 10^{18}$ cm^{-3} and 1.3$\times 10^{18}$ cm^{-3}, respectively. For the double layer the hole density is reduced to 1.1$\times 10^{18}$ cm^{-3} for the first oscillator. For the sixth oscillation, the density of hole showing values of 8.00 $\times 10^{19}$ cm^{-3} and 3.40 $\times 10^{19}$ cm^{-3} for the Glass/Nb_2O_5 and Glass/SnO_2 thin films then decreased to 1.83$\times 10^{19}$ cm^{-3} for the double layer. The decrease in the hole density of the double layer can be attributed to native defects in the double layers or possibly to the recombination that occurred when the SnO_2 layer was added to Glass/Nb_2O_5 layer, where Glass/SnO_2 exhibits possibly more oxygen vacancies than Glass/Nb_2O_5 which can annihilate holes [80]. The literature data reported free carrier concentration and plasma frequency values that are one order of magnitude lower than our Glass/Nb_2O_5 thin film values [81]. Moreover, for double layer thin_films, the hole concentration value can be compared with the literature data which are of the same order of magnitude [82].

The hole bounded plasmon frequency showing values of 1.15 GHz and 1.35 GHz for Glass/Nb_2O_5 and Glass/SnO_2 respectively increased to 1.40 GHz for the double layer. At the

second oscillator of the double layers, the plasma frequency matches the dielectric data (ω_{pe2}) given in Table 4.8. The plasma frequency values are optimized in the range of 1.40 - 5.71 GHz for the double layer, so the double layer can be used as wave traps of at least six resonant frequencies which mean it is suitable for wireless transmission and satellite communications, including microwave communication [45]. The propagating signal can be transmitted through the film if its frequency is higher than that of the plasmon frequency. The increase in the reduced resonant frequency, bounded plasmon frequency and drift mobility of the $Glass/Nb_2O_5/SnO_2$ double layer indicates improved dielectric performance of the stacked layers.

Chapter Five

Conclusions

In this work, we have considered the possibility of preparing $SnNb_2O_6$ compounds by three methods. The methods which included laser welding, solid state reaction and thermal evaporation techniques were successful in producing the compound with different physical characteristics. Structural, electrical and optical investigations have shown the ability to produce the compound as single phased and as amorphous material. It is noticeable that $SnNb_2O_6$ compound exhibits various structural phases under modified sintering temperatures. The produced compound can exhibit high and low electrical conductivities depending on the preparation technique. The preparation technique provides selectively of the possible class of applications. In general $SnNb_2O_6$ is found to be ideal material for use as radiowave and microwave resonators. They show negative conductivity in the microwave frequency domain. Thin film form of this material displayed energy band gap of ~ 3.5 eV. The modeling of the dielectric dispersion in the samples prepared by TE technique indicated that the films exhibit plasmon frequency in the range of 1.4-5.7 GHz, nominating the samples for use in 4G/5G mobile technologies.

Far from the novel features of the obtrained compound, some series consideration need to be mentioned. One of the major problems observed in the laser welding technique was optimization of large size samples. It was not possible to achieve samples of sizes larger than 0.2 cm. In addition, powder type alloys need to be treated via solid state reaction procedure to get effectively usable pellets. It is also worth mentioning that, samples prepared by SSR technique subjected to high sintering temperature above 1300°C display smaller crystallite sizes, larger

larger strains and higher defect densities. Still future works are needed to obtain enhanced structural and electrical properties of $SnNb_2O_6$ compound.

References

[1] Qasrawi, A. F., Abdalghafour, M. A., & Mergen, A. (2021). Tungsten doped $Bi_{1.5}Zn_{0.92}Nb_{1.5}O_{6.92}$ ceramics designed as radio/microwave band pass/reject filters. Microwave and Optical Technology Letters, 63(4), 1101-1105.

[2] Qasrawi, A. F., Kmail, B. H., & Mergen, A. (2012). Synthesis and characterization of $Bi_{1.5}Zn_{0.92}Nb_{1.5-x}Sn_xO_{6.92-x/2}$ pyrochlore ceramics. Ceramics International, 38(5), 4181-4187.

[3] Shi, F., Wang, J., & Sun, H. (2016). Influence of annealing time on microstructure and dielectric properties of $(Ba_{0.3}Sr_{0.7})(Zn_{1/3}Nb_{2/3})O_3$ ceramic thin films prepared by sol–gel method. *Journal of Materials Science: Materials in Electronics*, *27*(5), 4607-4612.

[4] Qasrawi, A. F., Sahin, E. İ., Emek, M., Kartal, M., & Kargin, S. (2019). Structural and dielectric performance of the $Ba_{(}Zn_{1/3}Nb_{2/3-x}Sb_x)O_3$ perovskite ceramics. Materials Research Express, 6(9), 095095.

[5] Krishnamoorthy, T., Tang, M. Z., Verma, A., Nair, A. S., Pliszka, D., Mhaisalkar, S. G., & Ramakrishna, S. (2012). A facile route to vertically aligned electrospun SnO_2 nanowires on a transparent conducting oxide substrate for dye-sensitized solar cells. Journal of Materials Chemistry, 22(5), 2166-2172.

[6] Szyszka, B., Dewald, W., Gurram, S. K., Pflug, A., Schulz, C., Siemers, M., ... & Ulrich, S. (2012). Recent developments in the field of transparent conductive oxide films for spectral selective coatings, electronics and photovoltaics. Current Applied Physics, 12, S2-S11.

[7] Tsai, M. Y., Bierwagen, O., & Speck, J. S. (2016). Epitaxial Sb-doped SnO_2 and Sn-doped In_2O_3 transparent conducting oxide contacts on GaN-based light emitting diodes. Thin Solid Films, 605, 186-192.

[8] Yu, H. K., Kim, S., Koo, B., Jung, G. H., Lee, B., Ham, J., & Lee, J. L. (2012). Nano-branched transparent conducting oxides: beyond the brittleness limit for flexible electrode applications. Nanoscale, 4(21), 6831-6834.

[9] Messad, A., Bruneaux, J., Cachet, H., & Froment, M. (1994). Analysis of the effects of substrate temperature, concentration of tin chloride and nature of dopants on the structural and electrical properties of sprayed SnO_2 films. Journal of materials science, *29*(19), 5095-5103.

[10] Kim, H., & Pique, A. (2004). Transparent conducting Sb-doped SnO_2 thin films grown by pulsed-laser deposition. Applied physics letters, 84(2), 218-220.

[11] Ravichandran, K., Muruganantham, G., & Sakthivel, B. (2009). Highly conducting and crystalline dobly doped tin oxide films fabricated using a low-cost and simplified spray technique. Physica B: Condensed Matter, 404(21), 4299-4302.

[12] Kasar, R. R., Deshpande, N. G., Gudage, Y. G., Vyas, J. C., & Sharma, R. (2008). Studies and correlation among the structural, optical and electrical parameters of spray-deposited tin oxide (SnO_2) thin films with different substrate temperatures. Physica B: Condensed Matter, 403(19-20), 3724-3729.

[13] Dubau, L., Maillard, F., Chatenet, M., Cavaliere, S., Jiménez-Morales, I., Mosdale, A., & Mosdale, R. (2020). Durability of alternative metal oxide supports for application at a proton-exchange membrane fuel cell cathode—Comparison of antimony-And niobium-doped tin oxide. *Energies*, *13*(2), 403.

[14] Elangovan, E., Shivashankar, S. A., & Ramamurthi, K. (2005). Studies on structural and electrical properties of sprayed SnO2: Sb films. Journal of Crystal Growth, 276(1-2), 215-221.

[15] Usha, N., Sivakumar, R., Sanjeeviraja, C., & Arivanandhan, M. (2015). Niobium pentoxide (Nb_2O_5) thin films: rf Power and substrate temperature induced changes in physical properties. Optik-International Journal for Light and Electron Optics, 126(19), 1945-1950.

[16] Salim, E. T., Ismail, R. A., & Halbos, H. T. (2019). Growth of Nb_2O_5 film using hydrothermal method: effect of Nb concentration on physical properties. Materials Research Express, 6(11), 116429.

[17] Qasrawi, A. F. (2005). Refractive index, band gap and oscillator parameters of amorphous GaSe thin films. Crystal Research and Technology: Journal of Experimental and Industrial Crystallography, 40(6), 610-614.

[18] Li, Y. X., Cao, Y., Wang, M., Xu, Z. L., Zhang, H. Z., Liu, X. W., & Li, Z. (2018). Novel high-flux polyamide/TiO2 composite nanofiltration membranes on ceramic hollow fibre substrates. Journal of Membrane Science, 565, 322-330.

[19] Kim, H. K., & Kim, S. H. (2019). Effect of hydrothermal aging on the optical properties of precolored dental monolithic zirconia ceramics. The Journal of prosthetic dentistry, 121(4), 676-682.

[20] Zhang, Z., Xu, S., Huang, J., Zhao, D., & Zhao, G. (2020). Straightforward synthesis and molecular structure optimization of novel SiZrBOC ceramic precursor via sol-gel and solvothermal approach. Ceramics International, 46(3), 3866-3874.

[21] Nikzad, L., Majidian, H., Ghofrani, S., & Ebadzadeh, T. (2018). Sintering behavior and microwave dielectric properties of $MgTiO_3$ obtained from coprecipitation method with additives. International Journal of Applied Ceramic Technology, 15(2), 569-574.

[22] Matsuo, H., Katayama, M., Minegishi, T., Yamada, T., Kudo, A., & Domen, K. (2019). Impact of lattice defects on water oxidation properties in $SnNb_2O_6$ photoanode prepared by pulsed-laser deposition method. Journal of Applied Physics, 126(9), 094901.

[23] Liu, M., Li, P., Cui, X., Cheng, L., Hu, Y., & Chen, W. (2021, March). Pt-Nb_2O_5-SnO_2 Composite Ceramics Competitive for Cost-Effective Room-Temperature Hydrogen Sensing. In Journal of Physics: Conference Series (Vol. 1838, No. 1, p. 012014). IOP Publishing.

[24] A. Rodrigues, T., Falsetti, P. H., Del Duque, D. M., da Silva, G. T., F. Lopes, O., Avansi, W & R. de Mendonça, V. (2021). A Versatile Nb2O5/SnO2 Heterostructure for Different Environmental Purposes: Water Treatment and Artificial Photosynthesis. ChemCatChem, 13(2), 730-738.

[25] Kohli, R., & Mittal, K. L. Developments in Surface Contamination and Cleaning, Volumes 1–12.

[26] Karim, K. M. R., Ong, H. R., Abdullah, H., Yousuf, A., Cheng, C. K., & Khan, M. M. R. (2018). Photoelectrochemical reduction of carbon dioxide to methanol on p-type $CuFe_2O_4$ under visible light irradiation. International Journal of Hydrogen Energy, 43(39), 18185-18193.

[27] Kittel, C., McEuen, P., & McEuen, P. (1996). Introduction to solid state physics (Vol. 8, pp. 105-130). New York: Wiley.

[28] Warren, B. E. (1990). X-ray Diffraction. Courier Corporation.

[29] Simeonova, P. P., Opopol, N., & Luster, M. I. (Eds.). (2007). Nanotechnology--toxicological issues and environmental safety (p. 232). Dordrecht, Netheralnds: Springer.

[30] Peng, W., Li, L., Yu, S., Zheng, H., & Yang, P. (2020). Structure, binding energy and optoelectrical properties of p-type CuI thin films: The effects of thickness. Applied Surface Science, 502, 144424.

[31] Al Garni, S. E., & Qasrawi, A. F. (2017). Effect of Indium nano-sandwiching on the structural and optical performance of ZnSe films. Results in physics, 7, 4168-4173.

[32] Shetty, M. N. (2013). Dislocations and mechanical behaviour of materials. PHI Learning Pvt. Ltd..

[33] Kuzel, R., Mittemeijer, E. J., & Welzel, U. (2006). Proceedings of the Ninth European Powder Diffraction Conference (EPDIC 9). In EPDIC 9. Oldenbourg Wissenschaftsverlag.

[34] Ershov, M., Liu, H. C., Li, L., Buchanan, M., Wasilewski, Z. R., & Jonscher, A. K. (1998). Negative capacitance effect in semiconductor devices. IEEE Transactions on Electron devices, 45(10), 2196-2206.

[35] Khusayfan, N. M., Qasrawi, A. F., & Khanfar, H. K. (2018). Design and electrical performance of CdS/Sb_2Te_3 tunneling heterojunction devices. Materials Research Express, *5*(2), 026303.

[36] Khanfar, H. K., Qasrawi, A. F., & Shehada, S. R. (2019). Negative Capacitance Effect in Ag/α-In_2Se_3/CdS/CdSe/C Dual Band Stop Filters. Journal of Electronic Materials, 48(1), 244-251.

[37] Nasri, S., Megdiche, M., & Gargouri, M. (2016). DC conductivity and study of AC electrical conduction mechanisms by non-overlapping small polaron tunneling model in LiFeP2O7 ceramic. Ceramics International, 42(1), 943-951.

[38] Ghosh, A. (1990). Frequency-dependent conductivity in bismuth-vanadate glassy semiconductors. Physical review B, 41(3), 1479.

[39] Qasrawi, A. F., & Khanfar, H. K. (2020). Al/MoO_3/ZnPc/Al Broken Gap Tunneling Hybrid Devices Design for IR Laser Sensing and Microwave Filtering. IEEE Sensors Journal, 20(24), 14772-14779.

[40] Makarov, S. N., Ludwig, R., & Bitar, S. J. (2019). Practical electrical engineering. Springer International Publishing.

[41] Fox, M. (1970). Optical properties of solids.

[42] Holgate, S. A. (2021). Understanding solid state physics. cRc Press.

[43] Kittel, C., McEuen, P., & McEuen, P. (1996). Introduction to solid state physics (Vol. 8, pp. 105-130). New York: Wiley.

[44] Fukuda, M. (1998). Optical semiconductor devices (Vol. 46). John Wiley & Sons.

[45] Qasrawi, A. F. (2019). EFFECT OF Y, Au AND YAu NANOSANDWICHING ON THE STRUCTURAL, OPTICAL AND DIELECTRIC PROPERTIES OF ZnSe THIN FILMS.

[46] Dresselhaus, M., Dresselhaus, G., Cronin, S. B., & Souza Filho, A. G. (2018). Solid State Properties (p. 329). Springer.

[47] Attwood, D. (2000). Soft x-rays and extreme ultraviolet radiation: principles and applications. Cambridge university press.

[48] Park, H., Lee, D., & Song, T. (2019). High capacity monoclinic Nb_2O_5 and semiconducting NbO_2 composite as high-power anode material for Li-Ion batteries. Journal of Power Sources, 414, 377-382.

[49] Rodríguez- Aranda, M. C., Alanis, J., Ojeda- Galván, H. J., Villabona-Leal, E. G., Rodríguez, A. G., Quintana, M., & Navarro- Contreras, H. R. (2021). One-pot hydrothermal

synthesis and formation mechanism of $SrNb_2O_6$-$Sr_2Nb_2O_7$-$Sr5Nb_4O_{15}$ lamellar perovskites in highly concentrated NaOH solutions. Ceramics International.

[50] Rani, R. A., Zoolfakar, A. S., O'Mullane, A. P., Austin, M. W., & Kalantar-Zadeh, K. (2014). Thin films and nanostructures of niobium pentoxide: fundamental properties, synthesis methods and applications. Journal of Materials Chemistry A, 2(38), 15683-15703.

[51] El Radaf, I. M., Hameed, T. A., & Dahy, T. M. (2019). Synthesis, structural, linear and nonlinear optical properties of chromium doped SnO2 thin films. Ceramics International, 45(3), 3072-3080.

[52] Dhinakar, K. G., Selvalakshmi, T., Sundar, S. M., & Bose, A. C. (2016). Structural, optical and impedance properties of SnO_2 nanoparticles. Journal of Materials Science: Materials in Electronics, 27(6), 5818-5824.

[53] Matar, S. F., Subramanian, M. A., & Etourneau, J. (2014). Pressure induced metallization of fordite $SnNb_2O_6$ from first principles. Computational materials science, 84, 355-359.

[54] Qasrawi, A. F., & Zyoud, H. M. (2020). Dielectric dispersion at the Mn/ZnPc interfaces. physica status solidi (b), 257(6), 2000089.

[55] Huang, S., Wang, C., Sun, H., Wang, X., & Su, Y. (2018). Steering Charge Kinetics of Tin Niobate Photocatalysts: Key Roles of Phase Structure and Electronic Structure. Nanoscale research letters, 13(1), 1-12.**55]**

[56] Bhaskar, A., & Murthy, S. R. (2013). Effect of sintering temperature on the electrical properties of Mn (1%) added MgCuZn ferrites by microwave sintering method. Journal of Materials Science: Materials in Electronics, 24(9), 3292-3298.

[57] Hankare, P. P., Jadhav, S. D., Sankpal, U. B., Chavan, S. S., Waghmare, K. J., & Chougule, B. K. (2009). Synthesis, characterization and effect of sintering temperature on magnetic properties of MgNi ferrite prepared by co-precipitation method. Journal of alloys and compounds, 475(1-2), 926-929.

[58] Qasrawi, A. F. (2019). EFFECT OF INSERTION OF ALUMINUM NANOSHEETS ON THE STRUCTURAL, OPTICAL AND DIELECTRIC PROPERTIES OF STACKED LAYERS OF SELENIUM.

[59] Montecinos, S., Cuniberti, A., & Sepúlveda, A. (2008). Grain size and pseudoelastic behaviour of a Cu–Al–Be alloy. Materials Characterization, 59(2), 117-123.

[60] Qasrawi, A. F., & Zyoud, H. M. (2020). Ytterbium induced structural phase transitions and their effects on the optical and electrical properties of ZnPc thin films. Optical and Quantum Electronics, 52(11), 1-12.

[61] Alassi, A., Benammar, M., & Brett, D. (2017). Quartz crystal microbalance electronic interfacing systems: A review. Sensors, 17(12), 2799.

[62] Nworji, G. C., Okpala, U. V., Okereke, N. A., & Okoye, P. U. (2020). Effect of Time Factor on the Battery Voltage State of Charge from Foot Beats Piezoelectric System. Asian Journal of Research and Reviews in Physics, 53-64.

[63] Bhaumik, A., Das, A., Mishra, A. K., Shaw, A., Yadav, A., & Roy, S. (2017, April). Non-conventional energy sources using piezoelectric crystal for wearable electronics. In 2017 1st International Conference on Electronics, Materials Engineering and Nano-Technology (IEMENTech) (pp. 1-4). IEEE.

[64] Qasrawi, A. F., Abdalghafour, M. A., & Mergen, A. (2021). Tungsten doped $Bi_{1.5}Zn_{0.92}Nb_{1.5}O_{6.92}$ ceramics designed as radio/microwave band pass/reject filters. Microwave and Optical Technology Letters, 63(4), 1101-1105.

[65] Qasrawi, A., Latifah, A., & Sabah, A. (2021). Yb/inse/sb2te3/au broken gap heterojunction devices designed as current rectifiers, tunable mos capacitors and gigahertz microwave cavities.

[66] Qasrawi, A. F., & Aloushi, H. D. (2019). Formation, negative capacitance and negative conductance effects in Selenium stacked layers sandwiched with Ag nanosheets. Materials Research Express, 6(8), 086435.

[67] Gloystein, A., Möller, C., & Nilius, N. (2019). Negative differential conductance in the electron-transport through copper-rich cuprous oxide thin films. New Journal of Physics, 21(11), 113026.

[68] Shaheen, A., Ali, M., Othman, W., & Tit, N. (2019). Origins of Negative Differential Resistance in N-doped ZnO Nano-ribbons: Ab-initio Investigation. Scientific reports, 9(1), 1-13.

[69] Kayed, T. S., & Qasrawi, A. F. (2020). Characterization of Au/As2Se3/MoO3/Ag hybrid devices designed for dual optoelectronic applications. Current Applied Physics, 20(1), 114-121.

[70] de Jesus, E. T., Moreira, A. J., Sá, M. C., Freschi, G. P. G., Joya, M. R., Li, M. S., & Paris, E. C. (2021). Potential of Nb2O5 nanofibers in photocatalytic degradation of organic pollutants. Environmental Science and Pollution Research, 1-15.

[71] Salim, E. T., Ismail, R. A., & Halbos, H. T. (2019). Growth of Nb_2O_5 film using hydrothermal method: effect of Nb concentration on physical properties. Materials Research Express, 6(11), 116429.

[72] Xu, B., Ren, X. G., Gu, G. R., Lan, L. L., & Wu, B. J. (2016). Structural and optical properties of Zn-doped SnO2 films prepared by DC and RF magnetron co-sputtering. Superlattices and Microstructures, *89*, 34-42.

[73] Harshavardhan, V., Kumar, R. J., Nagaraju, P., & Vijayakumar, Y. Structural, electrical optical and gas sensing properties of nanostructured pure SnO2 and Mg doped SnO2 thin films.

[74] Ali, H. M., & Hakeem, A. M. A. (2015). Characterization of n and p-type $(SnO_2)_x (ZnO)_{1-x}$ nanoparticles thin films. The European Physical Journal Applied Physics, 72(1), 10301.

[75] Qin, G., Li, D., Feng, Z., & Liu, S. (2009). First principles study on the properties of p-type conducting In: SnO2. Thin solid films, 517(11), 3345-3349.

[76] Alharbi, S. R., & Qasrawi, A. F. (2018). Optical dynamics in the Ag/α-Ga2S3 layer system. Materials Science in Semiconductor Processing, 83, 102-106.

[77] Nag, B. R. (2012). Electron transport in compound semiconductors (Vol. 11). Springer Science & Business Media.

[78] Chen, R. S., Wang, W. C., Lu, M. L., Chen, Y. F., Lin, H. C., Chen, K. H., & Chen, L. C. (2013). Anomalous quantum efficiency for photoconduction and its power dependence in metal oxide semiconductor nanowires. Nanoscale, 5(15), 6867-6873.

[79] Duffy, D. M., & Rutherford, A. M. (2009). Including electronic effects in damage cascade simulations. Journal of nuclear materials, 386, 19-21.

[80] Liu, A., Zhu, H., & Noh, Y. Y. (2019). Solution-processed inorganic p-channel transistors: Recent advances and perspectives. Materials Science and Engineering: R: Reports, 135, 85-100.

[81] Atta, A. A., El-Nahass, M. M., Hassanien, A. M., Elsabawy, K. M., Abd El-Raheem, M. M., Alhuthali, A., ... & Algamdi, M. S. (2017). Effect of thermal annealing on structural, optical and electrical properties of transparent Nb_2O_5 thin films. Materials Today Communications, 13, 112-118.

[82] Samizo, A., Minohara, M., Kikuchi, N., Bando, K. K., Aiura, Y., Mibu, K., & Nishio, K. (2020). Site-Selective Oxygen Vacancy Formation Derived from the Characteristic Crystal Structures of in Sn-Nb complex Oxides. arXiv preprint arXiv:2012.12921.

الملخص

طرق تحضير وبعض تطبيقات مركب اوكسيد النوبيوم القصدير

في هذه الرسالة ، قمنا بإعداد مركبات $SnNb_2O_6$ بثلاث طرق مختلفة. وهي على وجه التحديد ، من خلال تقنية اللحام بالليزر (WL) في وجود غاز N_2 و تقنية تفاعل الحالة الصلبة (SSR) وتقنية ترسيب الأغشية الرقيقة (TE). تم دراسة الخصائص التركيبية والبصرية والكهربائية للعينات الناتجة عن طريق تقنية حيود الأشعة السينية وتقنية التحليل الطيفي للمقاومة وتقنية قياس الطيف الضوئي . تضمنت طريقة التحضير بتقنية SSRعملية التلبيد بدرجات حرارة مختلفة في حدود 1000- 1400 درجة مئوية وأوقات تلبيد مختلفة من 2 - 6 ساعات. أظهر تحليل XRD حيود الأسعة السينية للعينات أن العينات المحضرة بواسطة تقنيات LW و SSR ذات طبيعة متعددة البلورات. أما عينة ال $SnNb_2O_6$ المحضرة على شكل غشاء رقيق أظهرت طبيعة غير متبلورة. بشكل عام ، تعرض عينات $SnNb_2O_6$ بنية متعددة الأطوار للتركيب البنائي , بحيث تعتمد المرحلة الهيكلية السائدة على تقنية التحضير و / أو درجة حرارة التلبيد. ويلاحظ أيضًا أنه بناءً على تقنية التحضير ، تتأثر المعلمات الهيكلية بما في ذلك الحجم البلوري والإجهاد الدقيق وأخطاء التراص وكثافة الخلع بشكل كبيرعلى طريقة التحضير. تم الحصول على عينات بأكبر حجم بلوري وأقل اجهاد وأقل كثافة عيوب بواسطة تقنية SSR عند درجة حرارة تلبيد 1300 درجة مئوية لمدة 3 ساعات. تم الوصول الى طور تركيبي مفرد لعينة ال $SnNb_2O_6$ وهو طورتقويم العظام (orthorhombic) بنفس الطريقة عند 1300 درجة مئوية حيث تم تلبيدها لمدة 3 ساعات. من ناحية أخرى ، أظهرت قياسات التحليل الطيفي للمقاومة أن العينات المحضرة بتقنية LW تعرض أعلى مقاومة في مجال التردد من 10-1800 ميجاهرتز. لوحظ التوصيل السالب للعينات المحضرة بواسطة تقنيات SSR و LW بالقرب من 1500 ميجاهرتز. بينما يُظهر طيف السعة للعينة المحضرة بتقنية اللحام بالليزر ظواهر الرنين- الطنين في مجال تردد الميكروويف. وظهرت نفس الظاهرة في العينات التي أعدت بتقنيتا ال SSR و TE في مدى تردد الموجات الراديوية. أشارت نمذجة أطياف السعة والموصلية إلى هيمنة طريقتي التوصيل : النفق الميكانيكي الكمي وتوصيل الحاجز المترابط (quantum mechanical tunneling and correlated barrier hopping conduction) في العينات. أشارت القياسات البصرية التي كانت ممكنة للعينات المحضرة بتقنية TE إلى وجود فجوتين سائدتين في نطاق الطاقة أعلى وأدنى من 3.0 الكترون فولت. بالإضافة إلى ذلك ، أظهرت نمذجة التوصيلية الضوئية للطبقات المكدسة التي تم إجراؤها بمساعدة نهج Drude-Lorentz للعينات

المحضرة بتقنية TE أن حركة الانجراف لـ $SnNb_2O_6$ زادت عند تكديس طبقة SnO_2 فوق طبقة $Glass/Nb_2O_5$, حيث تعرض الطبقات المكدسة للأغشية قيم تردد مناسبة لمرنان الميكروويف.